



CHORUS

This is the accepted manuscript made available via CHORUS. The article has been published as:

Renormalization group analysis for the quasi-one-dimensional superconductor $\text{BaFe}_{2}\text{S}_{3}$

Elio J. König, Alexei M. Tsvelik, and Piers Coleman

Phys. Rev. B **98**, 184517 — Published 27 November 2018

DOI: [10.1103/PhysRevB.98.184517](https://doi.org/10.1103/PhysRevB.98.184517)

Renormalization group analysis for the quasi-1D superconductor BaFe_2S_3

Elio J. König,¹ Alexei M. Tsvelik,² and Piers Coleman^{1,3}

¹*Department of Physics and Astronomy, Rutgers University, Piscataway, New Jersey, 08854, USA*

²*Condensed Matter Physics and Materials Science Division,
Brookhaven National Laboratory, Upton, NY 11973-5000, USA*

³*Department of Physics, Royal Holloway, University of London, Egham, Surrey TW20 0EX, UK*
(Dated: October 29, 2018)

Motivated by the discovery of superconductivity in the two-leg, quasi-one dimensional ladder compound, BaFe_2S_3 we present a renormalization group study of electrons moving on a two leg, two orbital ladder, subjected to Hubbard repulsion U and Hund's coupling J . In our calculations, we adopt tightbinding parameters obtained from ab-initio studies on this material. At incommensurate filling, the long wavelength analysis displays four phases as a function of $0 \leq J/U < 1$. We show that a fully gapped superconductor is stabilized at sufficiently large Hund's coupling, the relative phases at the three Fermi points are “+,-,-”. By contrast, when the system is tuned to half filling, Umklapp scattering gives rise to Mott insulating phases. We discuss the general implications of our study for the broad class of iron-based superconductors.

PACS numbers: 75.50.Bb, 74.70.Xa, 71.10.Pm

I. INTRODUCTION

The origin of the superconducting phase of iron pnictides and iron chalcogenides remains an open and fascinating puzzle. The robust nature of iron-based superconductivity, found in both tetrahedral iron-pnictide and iron-selenide structures, despite a wide variation in Fermi surface geometries and crystal structures, is particularly striking[1–4]. The transition temperatures appear to be broadly independent of whether the particular compound displays hole pockets, electron pockets or both types of carrier. In view of substantial on-site Coulomb repulsion, this makes the quest for a generic pairing mechanism particularly challenging. Moreover, superconductivity has been reported in systems in both tetragonal and orthorhombic phases.

A particularly exotic example of this superconducting robustness within the zoo of iron-based materials is BaFe_2S_3 under pressure [5]. While the sulfide shares the same staggered tetrahedral structure as its quasi-two dimensional (q2D) cousins, with a band of delocalized d-electrons forming between Fe^{2+} ions, here the tetrahedra are organized into two-leg ladders, forming a quasi-one dimensional (q1D) structure (see Fig. 1). One of the fascinating aspects of this system, is that it opens up the possibility of analyzing the physics of iron based superconductivity using the powerful tools of one-dimensional renormalization group and bosonization.

The experimentally observed phase diagram [6–8] resembles that of q2D materials, with a superconducting dome developing at the end point of an antiferromagnetic (AF) phase. A further analogy is the “stripe” ordering of spins, in the ladder system this corresponds to a ferromagnetic ordering on the rungs and AF ordering along the legs [5]. On the other hand, a major difference between BaFe_2S_3 and the q2D materials is the insulating nature of the antiferromagnet, which contrasts with the bad metal behavior in more conventional materials.

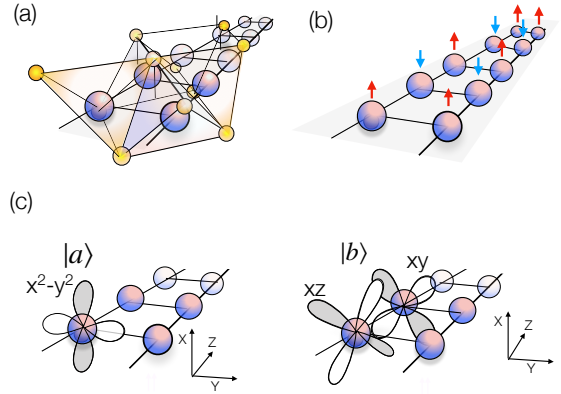


FIG. 1. (a) Ladder structure of BaFe_2S_3 shown running along Z axis, with sulphur tetrahedra (gold) surrounding iron atoms (blue). (b) Staggered antiferromagnetic “stripe” structure along ladder in magnetic phase at ambient pressure (c) Following ab-initio calculations [9, 10] we consider an effective two-orbital tight binding model composed from the $d_{x^2-y^2} \equiv |a\rangle$ orbital and a $|b\rangle$ orbital composed of a superposition of d_{xz} and d_{xy} orbitals.

Three years after the discovery of superconductivity in BaFe_2S_3 theoretical studies of this novel superconductor are still relatively sparse. Two groups [9, 10] reported ab-initio calculations extracting an effective two orbital tight binding model. The dispersion relation in ladder direction and the orbital content near the Fermi surface (see also Fig. 4) [11] qualitatively agree in both studies. A rough summary of energy scales follows: the Hubbard $U \sim 3eV$, the bandwidth (intraladder hopping) $\Lambda \sim 2eV$, the Hund's coupling $J \sim 0.5eV$, the interladder hopping $t_{\perp} \sim 0.25eV$. The effects of interactions on this compound are discussed in Ref. [9] based on the analysis of the Lindhard function, while the authors of Ref. [10] investigate the interplay of Hubbard and Hund's coupling

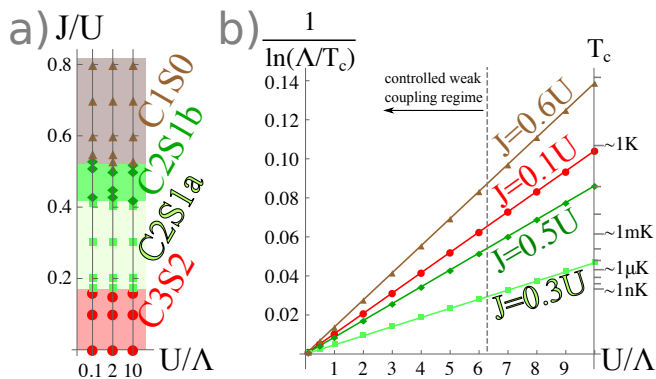


FIG. 2. Phase diagram and critical temperature as a function of U . As explained in the main text, the nature of the ground state depends on the ratio J/U , only. The numerical solutions of the RG equations presented here were obtained for Fermi velocities as defined by Fig. 4. Panel a): Phase diagram for three values of U/Λ , data points are marked by dots (C3S2), squares (C2S1a), diamonds (C2S1b) and triangles (C1S0) corresponding to four different phases in ascending order of J/U . Panel b): The critical temperature $T_c(U)$ associated to the instability of RG equations. Straight solid lines are obtained using Eq. (13) with $T_c(\Lambda)$ as the only numerical input, additional numerical solutions are again presented as dot, square, diamond and triangle, respectively. We used $\Lambda = \bar{v}/\tilde{a}$ and assumed $\Lambda \sim 1\text{eV}$ to estimate T_c in Kelvin on the right vertical axis.

using density matrix renormalization group. Both papers correctly reproduce the "striped" AF state, which was also reported in earlier density functional theory studies [12]. A slave spin approach [13] based on the tight-binding model of Ref. [9] reveals orbital selective correlations. The first order, pressure induced magnetic transition was recently scrutinized [14] for BaFe_2S_3 and related materials. We note that stripe order may also be understood in terms of a $J_1 - J_2$ AF Heisenberg model: As soon as the diagonal coupling J_2 exceeds $J_1/2$, stripe order is energetically favored over a Néel-type order [15]. Superconductivity is discussed qualitatively in Ref. [9] and the calculation of Ref. [10] indicates a pairing tendency in hole doped systems at sufficiently strong interactions. In a recent follow-up [16], the same group reports pairing tendencies in single-leg chains with the same orbital content and the importance of Hund's coupling was emphasized. It is important to realize, that density matrix renormalization group studies for multi-orbital Hamiltonian are numerically costly and thus restricted to small systems.

Motivated by these recent experimental and theoretical advances, here we present a weak-coupling renormalization group study of a two-orbital, two-leg ladder with on-site Hubbard and Hund interactions. The orbital content of Fermi-surface excitations is chosen in accordance with Refs. [9, 10] and we employ the same tight binding parameters as in [10] to determine the Fermi velocities at three pairs of Fermi momenta. A crucial step in our approach, is the reformulation of the onsite Coulomb and

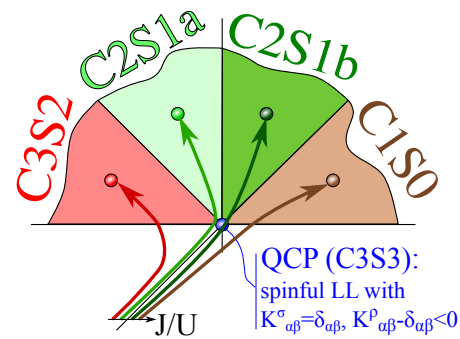


FIG. 3. Schematic summary of the RG flow obtained numerically in Figs. 8-11 of the Appendix. At the initial stage, coupling constants flow towards a quantum critical point (QCP), which in the present 1D study is just a spinful Luttinger liquid (LL) with three charge and three spin modes (C3S3). Near the QCP, the flows diverge towards four possible attractive fixed points (phases), discussed in Fig. 2. At intermediate J/U , the RG flow approaches the QCP very closely, it therefore slows down and T_c is suppressed in the phases C2S1a and C2S1b.

Hund's interactions as a set of eighteen interaction parameters g_μ ($\mu \in (1, 18)$) defining the strength of interaction between the left and right moving spin and charge currents in the various orbitals. From this formulation, we are able to construct a set of coupled RG equations that have the general form

$$\frac{dg_\mu(y)}{dy} = \beta_{\mu\nu\rho} g_\nu(y) g_\rho(y), \quad (1)$$

where $y = \ln \Lambda$ is the logarithm of the energy cut-off. Our analysis of coupled RG equations for the ladder model is the 1D analog of the parquet-RG approach to q2D iron based superconductors [17–19] and, being a weak coupling - long wavelength study it provides a complementary perspective to the strong coupling DMRG computations on finite ladders [10].

The key result of our paper is the identification of four stable ground-state phases which fan out from a central quantum critical point described by a gapless Luttinger liquid (LL). Crucially, it is the strength of the Hund's coupling which tunes between the four phases. (see figures 2 and 3). Moreover, by analyzing the effect of umklapp scattering at half-filling we can show that these phases emerge from a Mott insulating phase that develops at half-filling.

To characterize the excitation spectrum of these phases, we have used bosonization to perform a semiclassical strong-coupling analysis which permits a characterization of the gapless modes that dominate the quasi-long-range order. Following the convention of 1D ladder systems, we use the notation "CmSn" to describe a phase with m gapless boson modes in the charge sector and n gapless modes in the spin sector. The four stable phases can be summarized as follows:

- C1S0 ($J/U > 0.55$) Orbitorally selective singlet su-

perconductor, characterized by strong intraband pairing with relative phases $+, -, -$ on the three Fermi momenta.

- C2S1b ($J/U \in [0.45, 0.55]$) Singlet, equal sign, intraband superconductor at two Fermi momenta decoupled from a LL at the third Fermi momentum.
- C2S1a ($J/U \in [0.18, 0.42]$) Orbitaly ordered charge density wave decoupled from a LL.
- C3S2 ($J/U \leq 0.18$) Long range superconducting and charge density wave correlations stemming from one out of the three Fermi momenta.

The structure of the paper is as follows: The microscopic model is introduced in Sec. II, the RG analysis and the discussion of the rich phase diagram are presented in Sec. III. We conclude with a summary and outlook. Full details on the model and the RG calculation are included in the appendices A and B.

II. MODEL

In this section we present the model under investigation. At each rung of the ladder, see Fig. 1, there are eight degrees of freedom: the chain index $\tau = 1, 2$, the orbital quantum number $\gamma = a, b$ and the spin z-component $\sigma = \uparrow, \downarrow$. The corresponding electron annihilation operator at site j is then written $d_{\tau\gamma\sigma}(j)$. We incorporate the chain and orbital indices into a four-component spinor, defined for each site j and spin component σ as follows:

$$d_{\sigma}(j) = \begin{pmatrix} d_{1a\sigma}(j) \\ d_{1b\sigma}(j) \\ d_{2a\sigma}(j) \\ d_{2b\sigma}(j) \end{pmatrix}. \quad (2)$$

A. Kinetic term

The dispersion relations presented in Refs. [9, 10] are qualitatively similar to Fig. 4. For details of the tight binding model see Appendix A 1. The important, robust features of the model are as follows:

- 1) In the interval $k \in [0, \pi]$, there are two Fermi points of right movers at k_I, k_{II} and one left mover at $-k_{III}$. For each of them, time reversal symmetry imposes Fermi points of opposite velocity at the reversed momentum.
- 2) The excitations near k_{II} and k_{III} are even parity under reflections in the mirror plane running along the ladder ($Y \rightarrow -Y$), whereas the excitations near k_I are odd-parity under this reflection.
- 3) The excitations near $\pm k_{II}$ or $\pm k_{III}$ approximate pure orbital states a and b respectively, while excitations near $\pm k_I$ are in an orbital superposition ($|a\rangle \pm i|b\rangle)/\sqrt{2}$.

- 4) At half-filling the integration over filled states implies $k_I + k_{II} + k_{III} = 0$ (we took into account that crystal momenta of 0 and 2π are equivalent).

In the continuum limit, this motivates an expansion in low-energy modes. For convenience, we label the continuous position along the chain by $x_j = \tilde{a}j$ and set the lattice constant $\tilde{a} = 1$ everywhere in the paper. (Note that by using x , we have tacitly rotated the co-ordinate system relative to Fig. 1 and introduced $(x, y, z) = (Z, X, Y)$). In the continuum limit, we can factor out the rapidly varying components of the electron field, and decompose it into right (R) and left (L) moving components as follows:

$$\hat{d}_{\sigma}(x) = \sum_{\beta \in \{I, III\}} [e^{ik_{\beta}x} \Psi_{\beta} \hat{a}_{\beta\sigma}^R(x) + e^{-ik_{\beta}x} \Psi_{\beta}^* \hat{a}_{\beta\sigma}^L(x)] \quad (3)$$

where $a_{\beta\sigma}^{R,L}(x)$ corresponding to right and left-moving components of the fields and the three Fermi momenta are $k_{\beta} = (k_I, k_{II}, k_{III})$. The spinor components of the wavefunctions are

$$\begin{aligned} \Psi_I &= \begin{pmatrix} 1/\sqrt{2} \\ -1/\sqrt{2} \end{pmatrix}_{\tau} \otimes \begin{pmatrix} 1/\sqrt{2} \\ i/\sqrt{2} \end{pmatrix}_{\gamma} = \begin{pmatrix} 1/2 \\ i/2 \\ -1/2 \\ -i/2 \end{pmatrix}, \\ \Psi_{II} &= \begin{pmatrix} 1/\sqrt{2} \\ 1/\sqrt{2} \end{pmatrix}_{\tau} \otimes \begin{pmatrix} 1 \\ 0 \end{pmatrix}_{\gamma} = \begin{pmatrix} 1/\sqrt{2} \\ 0 \\ 1/\sqrt{2} \\ 0 \end{pmatrix}, \\ \Psi_{III} &= \begin{pmatrix} 1/\sqrt{2} \\ 1/\sqrt{2} \end{pmatrix}_{\tau} \otimes \begin{pmatrix} 0 \\ 1 \end{pmatrix}_{\gamma} = \begin{pmatrix} 0 \\ 1/\sqrt{2} \\ 0 \\ 1/\sqrt{2} \end{pmatrix}. \end{aligned} \quad (4)$$

The kinetic part of the long-wavelength Hamiltonian is then

$$H_{\text{kin}} = -iv_{\beta} \int dx [a_{\beta\sigma}^R \dagger \nabla_x a_{\beta\sigma}^R - a_{\beta\sigma}^L \dagger \nabla_x a_{\beta\sigma}^L]. \quad (5)$$

where we use an index notation for summation over the repeated variables $\beta = (I, II, III)$ and $\sigma = (\uparrow, \downarrow)$. The Fermi-velocities $v_{I,II,III}$ as well as the values $k_{I,II,III}$ are non-universal and may continuously vary as a function of the microscopic parameters.

B. Interaction terms

We assume a simplified model of onsite Hubbard and Hund interactions, $H_{\text{int}} = \sum_j H_U(j) + H_J(j)$, where the interactions at each site are

$$H_U(j) = \frac{U}{2} \sum_{\substack{\tau, \gamma, \sigma, \\ \gamma', \sigma'}} n_{\tau\gamma\sigma}(j) n_{\tau\gamma'\sigma'}(j), \quad (6a)$$

$$H_J(j) = -4J \sum_{\tau} \vec{S}_{\tau a}(j) \cdot \vec{S}_{\tau b}(j), \quad (6b)$$

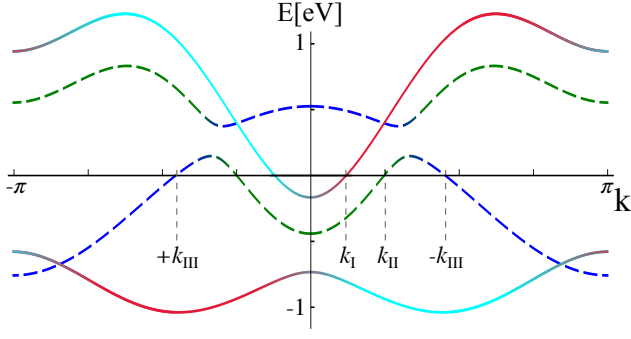


FIG. 4. Dispersion relation using the tight binding parameters determined in Ref. [10] for an applied pressure of 12.36 GPa and including next-nearest neighbor hopping. The dashed (solid) curves correspond to states which are symmetric (antisymmetric) under $y \rightarrow -y$ reflection and at the avoided crossing at $k \approx \pi/3$ ($k = 0$) the orbital character of the eigenstates changes. For the symmetric states, we use dark green to represent orbital $|a\rangle$ and blue for $|b\rangle$. For the antisymmetric states the superposition $[|a\rangle + i|b\rangle]/\sqrt{2}$ ($[|a\rangle - i|b\rangle]/\sqrt{2}$) is represented in red (cyan).

where the summation symbol \sum' excludes $(\gamma, \sigma) = (\gamma', \sigma')$ and we have introduced density and spin operators, defined as follows:

$$n_{\tau\gamma\sigma}(j) = d_{\tau\gamma\sigma}^\dagger(j)d_{\tau\gamma\sigma}(j), \quad (7)$$

$$\vec{S}_{\tau\gamma}(j) = \sum_{\sigma, \sigma'} d_{\tau\gamma\sigma}^\dagger(j) \left(\frac{\vec{\sigma}}{2} \right)_{\sigma, \sigma'} d_{\tau\gamma\sigma'}(j). \quad (8)$$

More complicated Hubbard-Kanamori interactions with non-equal intra- and interorbital repulsion do not alter the main conclusions of our study and are therefore discussed in Apps. A 2 and B 5. In the continuum limit, it is useful to represent the interaction term in terms of scalar

$$\mathcal{J}_{\alpha\beta}^r(x) = \sum_{\sigma} a_{\alpha\sigma}^r(x)^\dagger a_{\beta\sigma}^r(x), \quad (r \in \{R, L\}) \quad (9)$$

and vector currents

$$\vec{\mathcal{J}}_{\alpha\beta}^r(x) = \sum_{\sigma, \sigma'} a_{\alpha\sigma}^r(x)^\dagger \left(\frac{\vec{\sigma}}{2} \right)_{\sigma, \sigma'} a_{\beta, \sigma'}^r(x), \quad (10)$$

involving states near the Fermi points $\alpha, \beta = \text{I, II, III}$. Writing $H_{\text{int}} = \int dx \mathcal{H}_{\text{int}}(x)$ in terms of the Hamiltonian density, then

$$\begin{aligned} \mathcal{H}_{\text{int}}(x) = & \tilde{c}_{\alpha\beta}^\rho \mathcal{J}_{\alpha\beta}^R(x) \mathcal{J}_{\alpha\beta}^L(x) + \tilde{f}_{\alpha\beta}^\rho \mathcal{J}_{\alpha\alpha}^R(x) \mathcal{J}_{\beta\beta}^L(x) \\ & - \left[\tilde{c}_{\alpha\beta}^\sigma \vec{\mathcal{J}}_{\alpha\beta}^R(x) \cdot \vec{\mathcal{J}}_{\alpha\beta}^L(x) + \tilde{f}_{\alpha\beta}^\sigma \vec{\mathcal{J}}_{\alpha\alpha}^R(x) \cdot \vec{\mathcal{J}}_{\beta\beta}^L(x) \right], \end{aligned} \quad (11a)$$

where we have used an index summation on the indices α, β . The bare interaction constants are given by

$$\tilde{f}_{\alpha\beta}^\rho = \frac{U}{8} \begin{pmatrix} 0 & 3 & 3 \\ 3 & 0 & 4 \\ 3 & 4 & 0 \end{pmatrix}_{\alpha\beta}, \quad (11b)$$

$$\tilde{f}_{\alpha\beta}^\sigma = \frac{U}{2} \begin{pmatrix} 0 & 1 & 1 \\ 1 & 0 & 0 \\ 1 & 0 & 0 \end{pmatrix}_{\alpha\beta} + J \begin{pmatrix} 0 & 1 & 1 \\ 1 & 0 & 2 \\ 1 & 2 & 0 \end{pmatrix}_{\alpha\beta}, \quad (11c)$$

$$\tilde{c}_{\alpha\beta}^\rho = \frac{U}{8} \begin{pmatrix} 8 & 1 & 1 \\ 1 & 4 & 0 \\ 1 & 0 & 4 \end{pmatrix}_{\alpha\beta} - \frac{J}{4} \begin{pmatrix} 3 & 0 & 0 \\ 0 & 0 & 0 \\ 0 & 0 & 0 \end{pmatrix}_{\alpha\beta}, \quad (11d)$$

$$\tilde{c}_{\alpha\beta}^\sigma = \frac{U}{2} \begin{pmatrix} 0 & 1 & 1 \\ 1 & 4 & 0 \\ 1 & 0 & 4 \end{pmatrix}_{\alpha\beta} + J \begin{pmatrix} 1 & 0 & 0 \\ 0 & 0 & 0 \\ 0 & 0 & 0 \end{pmatrix}_{\alpha\beta}, \quad (11e)$$

see Appendix A 2 for derivation.

By convention [20], the diagonal elements of forward scattering amplitudes $\tilde{f}_{\alpha\beta}$ are chosen to vanish and are absorbed into the Cooper channel constants $\tilde{c}_{\alpha\beta}$. Completely chiral interactions of the form $(\mathcal{J}^R)_{\alpha\alpha}(\mathcal{J}^R)_{\beta\beta}$ will also be disregarded since they are not renormalized and do not renormalize the above couplings at one loop order. Formally, the itinerant approach assumes $\bar{v} = \sum_{\alpha} v_{\alpha}/3 \gg U/(2\pi)$ and we consider $U > J$.

C. Umklapp scattering

The effective low-energy Hamiltonian presented above is restricted to two-body interactions, which are marginal operators. Interactions involving a higher number of fermionic operators are generated during RG but are irrelevant near the non-interacting fixed point and therefore usually disregarded. However, as the strong coupling regime is approached such terms can become relevant.

An example of such a three-body interaction that encodes qualitatively new physics is given by umklapp scattering. It develops at commensurate filling, only, by means of the processes represented in Fig. 5. In the present model umklapp scattering is a three body interaction even at half filling in view of the aforementioned constraint $\sum_{\beta=\text{I}}^{\text{III}} k_{\beta} = 0$: Three right movers, one for each Fermi point, have to conspire and collectively transfer twice their total momentum (a crystal momentum) to the lattice. The difference between our model and more conventional Hubbard models, where umklapp scattering is typically a two body interaction, derives from the detailed band structure of Fig. 4.

Umklapp scattering implies the following terms, see Fig. 5

$$\mathcal{H}_{\text{umklapp}} \sim -gU \left[\prod_{\beta=\text{I}}^{\text{III}} \left(a_{\beta\sigma'}^R \dagger a_{\beta\sigma\beta}^L \right) e^{-i2k_{\beta}x} + \text{H.c.} \right]. \quad (12)$$

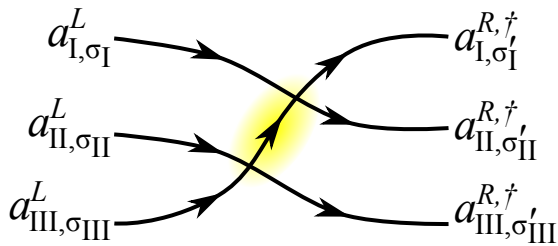


FIG. 5. For the model defined by Fig. 4, the umklapp process at half filling is a three body interaction. On the tree level, such processes are generated by means of two-body interactions and involve one virtual state away from the Fermi energy. Note that momentum is conserved modulo an inverse lattice vector only. This diagram indicates that the bare coupling is of the order U^2/\bar{v} .

Note that momentum is conserved only modulo the reciprocal lattice vector 2π . For the present model, there is a multitude of such interactions which differ by dissimilar spin indices (only the total spin is conserved). All of them have bare coupling constants $g_U \sim U^2/\bar{v}$.

III. RG ANALYSIS AT INCOMMENSURATE FILLING

In this section we present the RG analysis for the model defined in the previous section. We first concentrate on the case of incommensurate filling.

The low-energy theory introduced above is analogous to that of a three leg ladder [21–23], albeit with rather anisotropic interactions. It is known that the 18 independent parameters $\tilde{c}_{\alpha\beta}^{\sigma,\rho}$ and $\tilde{f}_{\alpha\beta}^{\sigma,\rho}$ form a closed set of running coupling constants under one-loop RG. The RG equations for a generic N-leg ladder were derived in Ref. [20]. Collecting the coupling constants into a single eighteen component vector $g_\mu = (\tilde{c}_{\alpha\beta}^\rho, \tilde{f}_{\alpha\beta}^\rho, \tilde{c}_{\alpha\beta}^\sigma, \tilde{f}_{\alpha\beta}^\sigma)_\mu$, the RG equations have the form of Eq. (1). Physically, the logarithmic scale factor $y = \ln(\Lambda/T)$ is determined by the ratio of the UV cut-off $\Lambda \sim \bar{v}$ and temperature T . The detailed form of the structure factors $\beta_{\mu\nu\rho}$ is given in App. B. Typically, the coupling constants diverge at a characteristic scale T_c . As a working definition we associate this scale with the onset of a symmetry broken phase, bearing in mind that strictly speaking, the divergence of one-loop RG in 1D marks the onset of the strong coupling regime and the development of gaps in some parts of the spectrum. In view of the simple structure of one-loop equations (1), the critical temperature $T_c(U)$ has the following functional form (see App. B)

$$T_c(U) = \Lambda \left(\frac{\Lambda}{T_c(\Lambda)} \right)^{-\frac{1}{\nu}}. \quad (13)$$

The reference scale $T_c(\Lambda)$ depends on J/U , therefore both the magnitude of U and of J/U determine the scale of the instability. In contrast, rescaling of the running scale and

coupling constants demonstrates that the phase diagram depends on the ratio J/U , only.

The RG equations were solved numerically using starting values defined by Eqs. (11) and Fermi velocities $v_I \approx 0.80eV$, $v_{II} \approx 0.86eV$, $v_{III} \approx 0.57eV$ as obtained from Fig. 4, restricting the values to the range $J/U \in [0, 0.8]$. We considered a large variety of $U/\bar{v} \in [0.02, 10]$, all leading to the same phase diagram as presented for three exemplary values of U/\bar{v} in Fig. 2. As we have mentioned above, the Fermi velocities are non-universal and depend on the chosen microscopic parameters. Therefore, a different set of Fermi velocities is explored in Appendix B, yielding similar results.

Our analysis identifies four different phases, as illustrated in figures 2 and 3. The distinguishing characteristic of each phase is the set of coupling constants that diverges and the signs of the divergences. Near the phase boundaries, large finite values and true divergencies are numerically indistinguishable, leading to minor numerical uncertainties in Fig. 2. In three out of four phases, several coupling constants diverge at the same scale preserving a finite, often universal, ratio. We derive these fixed ratios analytically, they imply an enhanced symmetry[24] at the attractive fix point and a connection to the integrable Gross-Neveu models discussed below. To determine the physical meaning of the phases, we bosonize the degrees of freedom

$$a_{\alpha,\sigma}^{R,L} \sim e^{i\sqrt{\pi}(\Phi_{\alpha,\sigma} \pm \Theta_{\alpha,\sigma})} \quad (14)$$

and perform a semiclassical strong coupling analysis near the instability. The latter allows to characterize gapful bosonic modes and to classify the operators displaying quasi-long range order. Following the lingo of 1D ladder systems, we use the notation “ $CmSn$ ” for a phase with m (n) massless bosons in the charge (spin) sector. Details on this procedure can be found in Appendix B. Here we summarize its outcome and discuss the phases in ascending order of J/U .

A. Phase C3S2

For small Hund’s coupling $J/U \lesssim 0.16$ only $\tilde{c}_{I,I}^\sigma$ diverges towards negative infinity (attraction in the Cooper channel), while all other coupling constants remain featureless. This is due to the small starting value of $\tilde{c}_{I,I}^\sigma = J$ which places the system close to a Cooper instability and in turn is due to the different orbital structure of left and right moving particles near k_I . A spin gap is developed near k_I while all excitations near $k_{II,III}$ remain gapless. Long-range correlations for singlet superconducting (SS) and also of charge density wave (CDW) order parameters occur in the C3S2 phase. When transformed back to the orbital and chain space, the superconducting order

parameter takes the form

$$\Delta \sim \Delta_I \Psi_I^R(x) [\Psi_I^L(x)]^T = \frac{\Delta_I}{4} \begin{pmatrix} 1 & -1 \\ -1 & 1 \end{pmatrix}_\tau \otimes \begin{pmatrix} 1 & -i \\ i & 1 \end{pmatrix}_\gamma. \quad (15)$$

We have included indices τ and γ in the matrix representation to clarify the direct product of chain and orbital spaces. Thus, the gap function contains a significant amount of orbital entanglement [25, 26] and has opposite sign along the rung and the steps of the ladder. As such it could be referred to as "d-wave", however, in 1D the notion of s-,d-, ... (p-,f-...) wave pairing is not well defined and we use the term even- (odd-) parity superconductivity instead. The gap function may be transformed to a real matrix by means of a $\pi/2$ -rotation about the z-axis in orbital space.

B. Phase C2S1a

At intermediate $0.16 \lesssim J/U \lesssim 0.41$ coupling constants involving only Fermi points k_{II} and k_{III} diverge, while those which involve Fermi point k_I are unaffected. The coupling constants scale as follows: $\tilde{c}_{\alpha\beta}^\sigma, \tilde{f}_{\alpha\beta}^\rho \rightarrow +\infty$ and $\tilde{c}_{\alpha\beta}^\rho, \tilde{f}_{\alpha\beta}^\sigma \rightarrow -\infty$ for $\alpha, \beta \in \{II, III\}$. For all starting values within phase C2S1a, the divergence of diagonal spin components is subdominant, such that $\tilde{c}_{\alpha\alpha}^\sigma/\tilde{c}_{II,III}^\sigma \rightarrow 0$, while the other coupling constants diverge with a universal, finite ratio near the fix point. This corresponds to the runaway flow in a certain, well defined direction of parameter space, such that the flow becomes effectively one-dimensional. In the Appendix, we expand the full RG equations about this ray and determine the ratios of divergence, amongst others $\tilde{c}_{II,III}^\rho = -\tilde{c}_{II,III}^\sigma/4$.

As compared to the three other phases, C2S1a displays repulsion in the Cooper channel. By means of the outlined semiclassical evaluation of the bosonized theory we find that the following bosonic modes are gapped

$$\Phi_{II}^\rho - \Phi_{III}^\rho, \Phi_{II}^s - \Phi_{III}^s, \Theta_{II}^s + \Theta_{III}^s, \quad (16)$$

where $\Phi_{\alpha}^{\rho,s} = (\Phi_{\alpha,\uparrow} \pm \Phi_{\alpha,\downarrow})/\sqrt{2}$ are charge and spin modes, respectively. The refermionization of bosonic degrees of freedom in these three sectors yields a Gross Neveu model and highlights the emergent $SO(6) \sim SU(4)$ symmetry, see App. B. Physically, the symmetry broken state corresponds to an orbitally ordered charge density wave. Returning to orbital and chain space, the order parameter is

$$O_{CDW}(x) = \begin{pmatrix} 1 & 1 \\ 1 & 1 \end{pmatrix}_\tau \otimes \gamma_y \otimes \mathbf{1}_\sigma e^{-i(k_{II}+k_{III}-\pi)x}. \quad (17)$$

C. Phase C2S1b

A rather narrow phase occurs for $0.42 \lesssim J/U \lesssim 0.53$. Again, coupling constants involving only Fermi points k_{II}

and k_{III} diverge, while those which involve Fermi point k_I are featureless. As in the C2S1a phase, the ratios of the divergent coupling constants is universal and the effective one-dimensional RG flow is derived in Appendix B. The divergent quantities are $\tilde{c}_{\alpha\beta}^{\rho,\sigma} \rightarrow -\infty$ and $\tilde{f}_{\alpha\beta}^\rho \rightarrow +\infty$, while $\tilde{f}_{\alpha\beta}^\sigma/\tilde{c}_{\alpha\alpha}^\sigma \rightarrow -0$. Amongst the various finite ratios, we remark that $\tilde{c}_{II,II}^\sigma/v_{II} = \tilde{c}_{III,III}^\sigma/v_{III}$ and $\tilde{c}_{II,III}^\rho = \tilde{c}_{II,III}^\sigma/4$. Such a phase was discussed in detail in Ref. [20] and contains two massless charged and one massless spin mode while

$$\Theta_{II}^s, \Theta_{III}^s, \Phi_{II}^\rho - \Phi_{III}^\rho, \quad (18)$$

are gapped. Again, the connection to an $SO(6)$ Gross Neveu model with enlarged symmetry can be obtained by refermionization in the three sectors in which the bosons condense. Physically, this phase corresponds to an intraband superconductor with gaps $\Delta_{II}, \Delta_{III}$ on the Fermi points k_{II}, k_{III} , in which $\Delta_{II}\Delta_{III} > 0$. In orbital and chain space, the spin singlet gap function is the sum of the following contributions

$$\Delta_{II} \Psi_{II}^R(x) [\Psi_{II}^L(x)]^T = \frac{\Delta_{II}}{2} \begin{pmatrix} 1 & 1 \\ 1 & 1 \end{pmatrix}_\tau \otimes \begin{pmatrix} 1 & 0 \\ 0 & 0 \end{pmatrix}_\gamma, \quad (19a)$$

$$\Delta_{III} \Psi_{III}^R(x) [\Psi_{III}^L(x)]^T = \frac{\Delta_{III}}{2} \begin{pmatrix} 1 & 1 \\ 1 & 1 \end{pmatrix}_\tau \otimes \begin{pmatrix} 0 & 0 \\ 0 & 1 \end{pmatrix}_\gamma. \quad (19b)$$

This superconducting state relies on intraorbital pairing and has the same sign along and across the ladder.

D. Phase C1S0

Finally, for $0.53 \lesssim J/U$ coupling constants involving any Fermi surface diverge. The Cooper coupling constants $\tilde{c}_{I,II}^{\sigma,\rho}, \tilde{c}_{I,III}^{\sigma,\rho} \rightarrow +\infty$ while all other $\tilde{c}_{\alpha\beta}^{\sigma,\rho} \rightarrow -\infty$. As in the C2S1b phase, for non-equal $\alpha \neq \beta$ the relationship $4\tilde{c}_{\alpha\beta}^\rho/\tilde{c}_{\alpha\beta}^\sigma \rightarrow 1$ holds. In the forward scattering channel $\tilde{f}_{\alpha\beta}^\sigma/\tilde{c}_{\alpha\beta}^{\sigma,\rho} \rightarrow 0$, while $\tilde{f}_{\alpha\beta}^\rho/\tilde{c}_{\alpha\beta}^\sigma$ approaches a small constant value for $\alpha \neq \beta$. The C1S0 phase is the analog of the C2S1b phase, with the only difference that now all three Fermi points display an instability towards a symmetry broken state and that intraband Cooper couplings diverge independently $\tilde{c}_{I,I}^\sigma/v_I \neq \tilde{c}_{II,II}^\sigma/v_{II} \neq \tilde{c}_{III,III}^\sigma/v_{III}$. The semiclassical analysis of the bosonized theory predicts spin gaps for all three spin modes Θ_i^s and charge gaps for the following two degrees of freedom.

$$\Phi_I^\rho - \Phi_{II}^\rho, \Phi_I^\rho - \Phi_{III}^\rho. \quad (20)$$

This state represents a fully gapped superconductor with gaps $\Delta_{I,II,III}$ and the charge modes lock in a manner such that

$$\text{sign}(\Delta_I\Delta_{II}) = \text{sign}(\Delta_I\Delta_{III}) = -\text{sign}(\Delta_{II}\Delta_{III}). \quad (21)$$

This follows from the positive signs of $\tilde{c}_{\text{I,III}}^{\sigma,\rho}$ and $\tilde{c}_{\text{I,II}}^{\sigma,\rho}$. Such a state may be called “s₊₋”, its gap function is the sum of Eqs. (15) and (19) with signs as imposed by Eq. (21). The only massless bosonic mode is the overall phase of the superfluid.

E. Discussion

In this section we include a discussion of the results, in particular of the superconducting phases.

1. RG flow

We begin with an examination of the RG flow. In this context it is useful to introduce the Luttinger parameter matrices $K_{\alpha\beta}^\rho \simeq \delta_{\alpha\beta} - 2\mathcal{C}_{\alpha\beta}^\rho$, $K_{\alpha\beta}^\sigma \simeq \delta_{\alpha\beta} + \mathcal{C}_{\alpha\beta}^\sigma/2$ with

$$K_{\alpha\beta}^{\rho,\sigma} = \frac{1}{\pi(v_\alpha + v_\beta)} \begin{pmatrix} \tilde{c}_{\text{I,I}}^{\rho,\sigma} & \tilde{f}_{\text{I,II}}^{\rho,\sigma} & \tilde{f}_{\text{I,III}}^{\rho,\sigma} \\ \tilde{f}_{\text{I,II}}^{\rho,\sigma} & \tilde{c}_{\text{II,II}}^{\rho,\sigma} & \tilde{f}_{\text{II,III}}^{\rho,\sigma} \\ \tilde{f}_{\text{I,III}}^{\rho,\sigma} & \tilde{f}_{\text{II,III}}^{\rho,\sigma} & \tilde{c}_{\text{III,III}}^{\rho,\sigma} \end{pmatrix}_{\alpha\beta}. \quad (22)$$

The RG flow can be subdivided into two stages, see Fig. 3: In a first step, $K_{\alpha\beta}^\sigma$ renormalizes down towards $\delta_{\alpha\beta}$ with $K_{\alpha\beta}^\rho$ being barely affected. Technically, this is due to terms of the standard Cooper form $d\mathcal{C}_{\alpha\beta}^\sigma/d\ln(\Lambda/T) = -(\mathcal{C}_{\alpha\beta}^\sigma)^2$ in the RG equations (B1). This state corresponds to a spinful LL with a non-interacting spin sector, as is customary. Its quantum critical nature is crucial in the present context as it represents a repulsive fixed point. Near the fixed point the flows diverge and, in the second stage, the system flows towards one of the four phases discussed above. By consequence, the set of coupling constants ($\tilde{c}_{\alpha\beta}^{\rho,\sigma}$, $\tilde{f}_{\alpha\beta}^{\rho,\sigma}$) in the infrared bears very little resemblance with the bare high-energy parameters. The pattern of interactions is completely reshuffled by many body effects. Notably, $K_{\alpha\alpha}^\rho - 1$ changes sign from intraband repulsion to intraband attraction for $\alpha = \text{II, III}$ ($\alpha = \text{I,II,III}$) in the superconducting phases C2S1b (C1S0) at lowest energies.

When a trajectory approaches the quantum critical point very closely, the flow slows down and T_c shoots up, this is the origin of the small T_c in the C2S1 phases. Furthermore, since small starting values of U are closer to $K_{\alpha\beta}^\sigma = \delta_{\alpha\beta}$ this also explains the dependence $T_c(U)$ as found in Eq. (13). We also note that the appearance of phases with gaps on a subset of the Fermi points is rather generic in N-leg ladders [20].

More specific technical observations follow. The trajectories towards C3S2 and C1S0 do not approach the QCP so closely leading to higher T_c . In particular, the vanishing bare value $\tilde{c}_{\text{I,I}}^\sigma$ at $J \rightarrow 0$ places the system close to the superconducting instability already. At larger J the repulsive flow near the QCP is driven by the RG equations (B1) which imply that the initially vanishing $\tilde{c}_{\text{II,III}}^{\sigma,\rho}$ are increasing in magnitude due to finite $\tilde{f}_{\text{II,III}}^{\rho,\sigma}$.

Finally, the divergence of $\tilde{c}_{\text{II,III}}^{\sigma,\rho}$ feeds back into the other channels, which are small at intermediate scales. This provides a mechanism to explain the transition near $J \sim U/2$ between phases C2S1a, in which $\tilde{c}_{\text{II,III}}^\sigma \rightarrow +\infty$, and C2S1b, in which $\tilde{c}_{\text{II,III}}^\sigma \rightarrow -\infty$. Namely, the RG equation for $\tilde{c}_{\text{II,III}}^\sigma$ contains the term $\tilde{c}_{\text{II,III}}^\sigma[\tilde{f}_{\text{II,III}}^{\rho,\sigma} - \tilde{f}_{\text{II,III}}^\sigma/2]$. The square bracket changes sign at $J = U/2$, see Eq. (11). It is important to stress that $\tilde{c}_{\text{II,III}}^{\sigma,\rho}$ have vanishing initial values, while the other interpocket Cooper interactions, $\tilde{c}_{\text{I,II}}^{\sigma,\rho}$ and $\tilde{c}_{\text{I,III}}^{\sigma,\rho}$ are repulsive (positive). Even after renormalization, $\tilde{c}_{\text{I,II}}^{\sigma,\rho}$ and $\tilde{c}_{\text{I,III}}^{\sigma,\rho}$ retain their positive sign, which ultimately leads to the s₊₋ superconductor in the C1S0 phase at largest Hund’s coupling J .

2. Physical implications and comparison to 2D

We now turn the attention towards the physical implications of the results. Based on Fig. 2 b), in which T_c is estimated in Kelvin based on a bandwidth $\Lambda \sim 1eV$, we conclude the following: First, none of the phases has an experimentally relevant T_c (above 1K) in the controlled weak coupling regime. We therefore extrapolate our analysis to larger interaction amplitudes under the assumption that the RG flow is at least qualitatively unchanged. Second, the phases with realistically observable T_c at intermediate coupling are C3S2 and C1S0, both of which have long-range superconducting correlations. The orbital order charge density wave C2S1a occurs at unrealistic energy scales, only.

It is interesting to compare the present 1D RG for the ladder material with previous studies of parquet RG [17, 18] designed for materials with cylindrical Fermi surfaces. Both approaches involve weak coupling theory, and the basic form of RG equations, Eq. (1), is the same, and thus Eq. (13) has an analogue in the 2D case. While the general observation that many body effects completely reshuffle the pattern of interaction constants persists to the higher dimensional systems, the clear two stage RG as observed in Figs. 8-11 seems to be specific to quasi 1D. In contrast with our q1D study, the 2D kinematics implies a “parquet-to-ladder” crossover scale given by $E_F \ll \Lambda$, below which the general weak coupling form Eq. (1) (parquet) takes the simpler form $\beta_{\mu\nu\rho} = \delta_{\mu\nu}\delta_{\nu\rho}\beta_\mu$ (ladder). Finally, an important common observation valid both for q2D and q1D is that intraband Coulomb interaction changes sign in the last stages of RG. Hence the RG predicts superconducting pairing states with sign changes between Fermi surfaces.

In view of this last point, it is often assumed that RG resolves the “Coulomb problem”: the question of how Coulomb repulsion is overcome in the superconducting state of iron pnictides and chalcogenides in a wide variety of different Fermi surface configurations, without a significant impact on the transition temperature. We recently investigated this issue in more detail [27] and came to the conclusion that generically RG is not sufficient to

explain the robustness of superconductivity against the Coulomb repulsion. In the present study the diverging Cooper attraction develops at the end of the scaling trajectories in channels with small or even vanishing bare couplings. The energy scale at which this occurs is strongly dependent on detailed microscopic interactions, suggesting a corresponding dependence of T_c on the microscopic details. Consequently, although RG is able to account for the appearance of pairing in a variety of different Fermi surface structures, it does not provide a natural explanation of the robustness of the superconducting transition temperatures in iron-based superconductors, and does not solve the Coulomb problem. This unsolved problem, which lies at the heart of the ubiquitous superconductivity in the family of iron-based superconductors remains an important challenge for the future.

IV. HALF-FILLING: UMKLAPP SCATTERING

The goal of this section is to qualitatively discuss umklapp operators, Eq. (12), by analyzing their scaling dimension d_u . We remind the reader that two electrons occupy each site at half filling, cf. Fig. 1, as a consequence umklapp scattering involves six fermionic operators. Due to the different spin structure discussed in Sec. II C, there is a total of $2^7 = 128$ umklapp terms. Their coupling constants are most conveniently parametrized by seven complex numbers $A^\rho, A_\alpha^s, B_\alpha^s$

$$\mathcal{H}_u = \text{Re}[A^\rho e^{i\sqrt{6\pi}\Theta_{\text{tot}}^\rho}] \prod_{\alpha=1}^{\text{III}} \text{Re}[A_\alpha^s e^{i\sqrt{2\pi}\Theta_\alpha^s} + B_\alpha^s e^{i\sqrt{2\pi}\Phi_\alpha^s}]. \quad (23)$$

We introduced $\Theta_{\text{tot}}^\rho = \sum_\alpha \Theta_\alpha^\rho / \sqrt{3}$ in the sector of total U(1) charge, the associated Luttinger parameter is $K_{\text{tot}}^\rho = \sum_{\alpha\beta} K_{\alpha\beta}^\rho / 3$. We discuss the scaling dimension of the umklapp operators in the vicinity of the five fixed points presented in Fig. 3, details are relegated to Appendix C. If umklapp scattering is RG relevant, it can lock the bosonic field Θ_{tot}^ρ . Then the system becomes an insulator with respect to the electromagnetic U(1) charge and all superconducting phases are suppressed.

At the repulsive quantum critical point, the scaling dimensions of the coupling constants are equal for all 128 umklapp terms and

$$d_u = (1 - 3K_{\text{tot}}^\rho)/2. \quad (24)$$

Umklapp operators are relevant only at strong repulsion $K_{\text{tot}}^\rho < 1/3$. We also remark that for an n -body interaction $d_u = 2 - n \stackrel{n=3}{=} -1$ at the non-interacting fixed point.

In the phase C3S2 the phase Θ_{I}^s condenses and therefore the product in Eq. (23) involves $\alpha = \text{II, III}$, only. Assuming $K_{\alpha\beta}^\sigma = \delta_{\alpha\beta}$ for $\alpha, \beta \in \{\text{II, III}\}$ the scaling dimension becomes

$$d_u = 1 - 3K_{\text{tot}}^\rho/2. \quad (25)$$

Mott localization occurs at intermediately strong coupling $K_{\text{tot}}^\rho < 2/3$, only.

The phases C2S1a and C2S1b are characterized by a spin gap near both Fermi points k_{II} and k_{III} . Effectively, the remaining umklapp terms have the form

$$\mathcal{H}_u = \text{Re}[A^\rho e^{i\sqrt{6\pi}\Theta_{\text{tot}}^\rho}] \text{Re}[A_{\text{I}}^s e^{i\sqrt{2\pi}\Theta_{\text{I}}^s} + B_{\text{I}}^s e^{i\sqrt{2\pi}\Phi_{\text{I}}^s}] \quad (26)$$

and (for $K_{\text{II}}^\sigma = 1$) the scaling dimension

$$d_u = 3(1 - K_{\text{tot}}^\rho)/2. \quad (27)$$

The transition occurs now at weak coupling, $K_{\text{tot}}^\rho = 1$. Note, however, that $K_{\alpha\beta}^\rho$ flows to attractive values near the fixed points. If Mott localization occurs C2S1a becomes a phase C1S0a in which the long range CDW correlations survive. Similarly, C2S1b becomes C1S0b, here superconducting correlations are suppressed but long range CDW correlations stemming from the Fermi point k_{I} persist.

Finally, the phase C1S0 has a spin gap at all Fermi momenta such that, effectively, $\mathcal{H}_u = \text{Re}[A^\rho e^{i\sqrt{6\pi}\Theta_{\text{tot}}^\rho}]$. The effective scaling dimension of the umklapp terms at the C1S0 fixed point is thus

$$d_u = 2 - 3K_{\text{tot}}^\rho/2, \quad (28)$$

and Mott localization occurs at $K_{\text{tot}}^\rho < 4/3$, i.e. formally even for attractive interaction. Then the system is fully gapped. In practice, the scaling dimension becomes relevant even before the C1S0 fixed point is reached. As we show explicitly in the Appendix, the dominant four umklapp operators have the form

$$\mathcal{H}_u = g_u \text{Re}[A^\rho e^{i\sqrt{6\pi}\Theta_{\text{tot}}^\rho}] \text{Re}[A^s e^{i\sqrt{6\pi}\Theta_{\text{rel}}^s}] \quad (29)$$

with $\Theta_{\text{rel}}^s = (\Theta_{\text{I}}^s - \Theta_{\text{II}}^s - \Theta_{\text{III}}^s) / \sqrt{3}$. Even in the weak coupling limit, the scaling dimension of these operators change sign from irrelevant to relevant before reaching the C1S0 fixed point, see Fig. 15 of the Appendix, and generate a C2S2 Mott insulating phase.

In order to illustrate the appearance of a Mott phase we numerically solve Eq. (1) along with $dg_u/dy = d_u(\{g_u\})g_u$ in the parameter regime of strong Hund's coupling, see Fig. 6. For sufficiently large U/Λ (e.g. $U/\Lambda \gtrsim 1.6$ for $J = 0.6U$) $d_u > 0$ even at the initial stage of RG. The divergence of the coupling constant is then dominated by the repulsive quantum critical fixed leading to

$$g_u(y) \approx g_u(0) e^{[1-3K_{\text{tot}}^\rho(y=0)]y/2}. \quad (30)$$

In Fig. 6, we employ a working definition of the Mott activation gap T_{Mott} by means of the scale $y_{\text{Mott}} = \ln(\Lambda/T_{\text{Mott}})$ at which $g_u(y_{\text{Mott}}) = (2\pi\Lambda)$ for starting value $g_u(0) = U^2/(2\pi\Lambda)$. For a density n away from the density of half filling n_0 , the divergence of g_u is cut at an energy scale $\bar{v}|n - n_0|$ leading to $T_{\text{Mott}}(n) = \sqrt{T_{\text{Mott}}(n_0)^2 - (\bar{v}|n - n_0|)^2}$. For clear illustration we

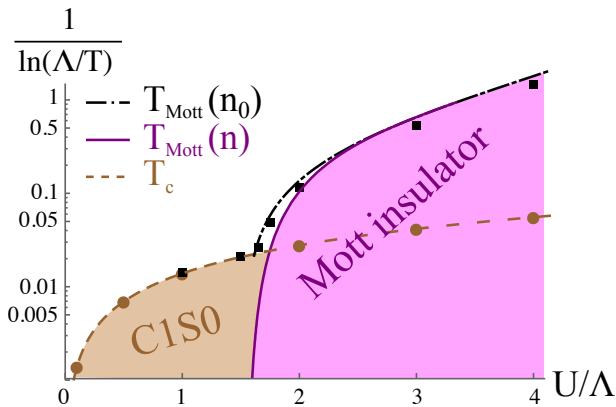


FIG. 6. Phase diagram at $J = 0.6U$, taking umklapp scattering into account. The quantity $U/\Lambda = U\tilde{a}/\bar{v}$ on the x-axis decreases with pressure, while the y-axis variable $1/\ln(\Lambda/T)$ increases with temperature. At large U/Λ and perfect commensuration, the superconducting T_c (numerical solution: brown dots; Eq. (13): dashed brown) always lies below the Mott localization temperature $T_{\text{Mott}}(n_0)$ defined heuristically by $g_u(y_{\text{Mott}}) = (2\pi\Lambda)$ (numerical solution: black squares; approximate solution, Eq. (30), valid for $U/\Lambda \gtrsim 1.6$: black dot-dashed). Away from half filling the Mott phase boundary is modified by the finite energy scale associated with doping (purple, here $(\bar{v}|n - n_0|/\Lambda)^2 = 0.3$) giving rise to a superconductor-insulator transition.

chose $(\bar{v}|n - n_0|/\Lambda)^2 = 0.3$, i.e. a rather large value, in Fig. 6. We note that using $\Lambda \simeq 1\text{eV}$, the phase boundaries of 6 occur at unrealistically low temperatures, which is a direct consequence of our weak coupling treatment. However, we conjecture that the qualitative outcome of our controlled calculations still holds in the strong coupling limit.

All in all, we conclude that Mott physics can be important for the present itinerant model. Umklapp scattering at half filling may be RG relevant near the attractive fixed points even though it is strongly irrelevant at the non-interacting limit.

V. SUMMARY AND OUTLOOK

In summary, we have investigated a single ladder for the quasi 1D iron based superconductor BaFe_2S_3 on the basis of the tightbinding model as suggested in Refs. [9, 10] and a simple onsite Hubbard and Hund interactions. The long-wavelength low-temperature physics was studied using an RG analysis of excitations close to the three pairs of Fermi points.

In the case of incommensurate filling the weak coupling RG analysis yields four phases depending on the ratio of Hund J to Hubbard U interactions, see Fig. 2. We have shown analytically and checked numerically that the absolute value of the interaction U at given J/U does not affect the ground state, but T_c increases rapidly as a function of U . In particular, a fully gapped supercon-

ductor is stabilized at sufficiently large ratio $J/U \gtrsim 0.53$. The intraband pairing gaps have signs $+, -, -$ on the three pairs of Fermi points and the critical temperature T_c is estimated to be of the order of 10 K for intermediately strong coupling. This theory provides a way to understand the conducting high pressure part of the experimental phase diagram [6]. In order to account for the observation of a Mott phase at low pressure we furthermore investigated umklapp scattering at half filling. In our three band model, umklapp processes are represented by three-body interactions and are hence irrelevant at weak coupling. However, we have shown that umklapp scattering does become relevant near some of the strong coupling fixed points. In this circumstance a charge gap develops, giving rise to a correlated insulator. Near commensurate filling these results indicate a Mott insulator-superconductor quantum phase transition (see Fig. 6) into a Hund's-driven superconducting phase at intermediate repulsion. This corroborates DMRG studies on very similar models [10, 16].

One of the fascinating aspects of our model, is that it is able to realize several different ground states which develop a dynamically enhanced symmetry, each characterized by different universal fixed-point ratios of the coupling constants. In the real 3D material the 1D renormalization group flows will be cut-off by interchain hopping, which is a relevant perturbation. In this spirit, the present study provides insight into the prediction towards certain superconducting and magnetic states that the real material inherits from its 1D building blocks.

There are various lessons that we have learnt that are relevant to the wider theoretical study of iron based superconductors. First, we have seen that the orbital structure of wave functions near the Fermi surface plays a crucial role in the formation of the order parameters. Second, the interorbital and orbital selective pairings are ubiquitous as soon as the orbital structure of the wave functions is taken into account. Third, even in weak coupling theories, the Hund's coupling has a dramatic impact. Finally, although RG studies enable us to understand the appearance of pairing in a wide variety of q1D Fermi surface structures, this pairing still requires a channel with a weak bare Coulomb interaction, and a generic mechanism which accounts for the weak bare repulsion in the iron-based superconductors is still needed.

VI. ACKNOWLEDGEMENTS

We thank Y. Komijani and P.-Y. Chang for useful discussions. E. König and P. Coleman were supported by the U.S. Department of Energy, Basic Energy Sciences, grant number DE-FG02-99ER45790. A. M. Tsvelik was supported by the U.S. Department of Energy (DOE), Division of Condensed Matter Physics and Materials Science, under Contract No. DE-SC0012704

Appendix A: Microscopic model

1. Tight binding model

In this Appendix we present further details on the tight binding model [10], which we use to obtain input parameters for the numerical integration of RG equations.

We consider a ladder as shown in Fig. 1. Our approach employs the following notation for the $2 \times 2 \times 2 = 8$ degrees of freedom at each site: a) Spin is represented by Pauli matrices σ . Spin eigenvalues are \uparrow, \downarrow . b) Pauli matrices in chain space are τ . We denote the chains by 1, 2 (upper, lower chain). Due to mirror symmetry along the chain direction, $\tilde{\tau} = \pm 1$ is a good quantum number which corresponds to parity eigenstates $\frac{1+\tilde{\tau}|2\rangle}{\sqrt{2}}$. c) Pauli matrices in orbital space are denoted by γ . The two orbitals are called a, b . The tight binding Hamiltonian contains nearest and next nearest rung hopping,

$$H_{\text{kin}} = \sum_{j\sigma} \left\{ [d_j^+ t_Z \mathbf{1}_\tau d_{j+1} + h.c.] + [d_j^+ t_{2Z} \mathbf{1}_\tau d_{j+2} + h.c.] \right. \\ \left. + [d_j^+ t_{Z+Y} \tau_1 d_{j+1} + h.c.] + [d_j^+ t_{2Z+Y} \tau_1 d_{j+2} + h.c.] \right. \\ \left. + d_j^+ t_Y \tau_1 d_j + \Delta d_j^+ \gamma_3 d_j - \mu d_j^+ d_j \right\}. \quad (\text{A1})$$

We note that t_μ with $\mu = Z, Y, Z+Y, 2Z, 2Z+Y$ are 2×2 matrices in orbital space and that their off-diagonal parts are antisymmetric and that we returned to the coordinate system (X, Y, Z) to make contact with Ref. [10]. We omitted the spin index for notational simplicity, following Ref. [10] t_Y is a diagonal matrix.

We introduce the Fourier transform $d_j = \frac{1}{N} \sum_k e^{ikj} d_k$ and perform a transformation in chain space into the basis of bonding/antibonding states. We define

$$d_k = \begin{pmatrix} d_{k,\tilde{\tau}=+1} \\ d_{k,\tilde{\tau}=-1} \end{pmatrix} = \frac{\tau_1 + \tau_3}{\sqrt{2}} \begin{pmatrix} c_{k,1} \\ c_{k,2} \end{pmatrix}, \quad (\text{A2})$$

where spin and orbital quantum numbers have been suppressed for convenience. This leads to the following result

$$H_{\text{kin}} = \sum_{\sigma=\uparrow,\downarrow, \tilde{\tau}=\pm 1} \int (dk) d_{k,\sigma,\tilde{\tau}}^+ \left[\sum_{i=0,2,3} h_{\tilde{\tau}}^{(i)} \gamma_i \right] d_{k,\sigma,\tilde{\tau}} \quad (\text{A3a})$$

where $d_{k,\sigma,\tilde{\tau}}$ are two spinors in orbital space, $\gamma_0 = \mathbf{1}_\gamma$ and we have introduced

$$h_{\tilde{\tau}}^{(0)} = 2 \cos(k) [t_Z^{(0)} + \tilde{\tau} t_{Z+Y}^{(0)}] + 2 \cos(2k) [t_{2Z}^{(0)} + \tilde{\tau} t_{2Z+Y}^{(0)}] \\ - \mu + \tilde{\tau} t_Y^{(0)} \quad (\text{A3b})$$

$$h_{\tilde{\tau}}^{(2)} = 2i \sin(k) [t_Z^{(2)} + \tilde{\tau} t_{Z+Y}^{(2)}] + 2i \sin(2k) [t_{2Z}^{(2)} + \tilde{\tau} t_{2Z+Y}^{(2)}] \quad (\text{A3c})$$

$$h_{\tilde{\tau}}^{(3)} = 2 \cos(k) [t_Z^{(3)} + \tilde{\tau} t_{Z+Y}^{(3)}] + 2 \cos(2k) [t_{2Z}^{(3)} + \tilde{\tau} t_{2Z+Y}^{(3)}] \\ + \Delta + \tilde{\tau} t_Y^{(3)}. \quad (\text{A3d})$$

We have also introduced $t_\mu^{(i)} = \text{tr}[t_\mu \gamma_i]/2$ with $\mu = Z, Y, Z+Y, 2Z, 2Z+Y$ and $i = 0, 2, 3$. In this notation, $h_{\tilde{\tau}}^{(2)}$ is real and the time reversal symmetry $\left[\sum_{i=0,2,3} h_{\tilde{\tau}}^{(i)} \gamma_i \right]^T = \left[\sum_{i=0,2,3} h_{\tilde{\tau}}^{(i)} \gamma_i \right]_{k \rightarrow -k}$ is apparent. The spectrum of the tight binding Hamiltonian is then

$$\epsilon_{\tilde{\tau},\gamma}(k) = h_{\tilde{\tau}}^{(0)} + \gamma \sqrt{(h_{\tilde{\tau}}^{(2)})^2 + (h_{\tilde{\tau}}^{(3)})^2}. \quad (\text{A4})$$

The plot of the spectrum for the parameters given in Eq. (3) of Ref. [10] is given in Fig. 4.

2. Interaction terms

Here we provide more details about the interaction terms. It is useful to disentangle interorbital from intraorbital contributions in the Hubbard interaction, even though we set $\tilde{U} = U$ in the main text. In the following $\mathcal{P}_{\gamma,\tau,\sigma}$ are projectors onto a given orbital, chain, and spin respectively.

$$H_U = U \sum_j \sum_{\gamma=a,b} \sum_{\tau=1,2} (d_{j,\uparrow}^\dagger \mathcal{P}_\gamma \mathcal{P}_\tau d_{j,\uparrow}) (d_{j,\downarrow}^\dagger \mathcal{P}_\gamma \mathcal{P}_\tau d_{j,\downarrow}) \quad (\text{A5})$$

$$H_{\tilde{U}} = \tilde{U} \sum_j \sum_{\tau=1,2} (d_{j,\uparrow}^\dagger \mathcal{P}_a \mathcal{P}_\tau \mathbf{1}_\sigma d_{j,\uparrow}) (d_{j,\downarrow}^\dagger \mathcal{P}_b \mathcal{P}_\tau \mathbf{1}_\sigma d_{j,\downarrow}) \quad (\text{A6})$$

As a next step, we carry out the long-wavelength expansion, Eq. (3), into the interaction terms of the Hamiltonian. As usual, the overall momentum conservation may be preserved in three different manners, corresponding to direct, exchange and Cooper channels.

a. Intraorbital Hubbard interaction We begin by rewriting the intraorbital Hubbard interaction, Eq. (A5) in terms of low-energy modes.

In the density channel we then obtain

$$H_U^{(0)} = \frac{U}{8} \int dx \sum_{\alpha=\text{II,III}} \left(\sum_r (a_{1,\uparrow}^{r,\dagger} a_{1,\uparrow}^r + 2a_{\alpha,\uparrow}^{r,\dagger} a_{\alpha,\uparrow}^r) \right) \\ \times \left(\sum_{r'} (a_{1,\downarrow}^{r',\dagger} a_{1,\downarrow}^{r'} + 2a_{\alpha,\downarrow}^{r',\dagger} a_{\alpha,\downarrow}^{r'}) \right), \quad (\text{A7a})$$

while in the exchange channel the interaction takes the form

$$H_U^{(X)} = -\frac{U}{8} \int dx \sum_{\alpha=\text{II,III}} \left(\sum_r (a_{1,\uparrow}^{r,\dagger} a_{1,\downarrow}^r + 2a_{\alpha,\uparrow}^{r,\dagger} a_{\alpha,\downarrow}^r) \right) \\ \times \left(\sum_{r'} (a_{1,\downarrow}^{r',\dagger} a_{1,\uparrow}^{r'} + 2a_{\alpha,\downarrow}^{r',\dagger} a_{\alpha,\uparrow}^{r'}) \right). \quad (\text{A7b})$$

Finally, in the Cooper channel we obtain

$$H_U^{(C)} = \frac{U}{8} \int dx \sum_{\alpha=\text{II,III}} \left(\sum_r (a_{1,\uparrow}^{r,\dagger} a_{1,\downarrow}^{-r,\dagger} + 2a_{\alpha,\uparrow}^{r,\dagger} a_{\alpha,\downarrow}^{-r,\dagger}) \right) \\ \times \left(\sum_{r'} (a_{1,\downarrow}^{r',\dagger} a_{1,\uparrow}^{-r',\dagger} + 2a_{\alpha,\downarrow}^{r',\dagger} a_{\alpha,\uparrow}^{-r',\dagger}) \right). \quad (\text{A7c})$$

b. Interorbital Hubbard interaction Next we look at the interorbital Hubbard term, Eq. (A6). In the density channel we obtain

$$H_{\tilde{U}}^{(0)} = \frac{\tilde{U}}{8} \int dx \left(\sum_{\sigma,r} (a_{I,\sigma}^{r,\dagger} a_{I,\sigma}^r + 2a_{II,\sigma}^{r,\dagger} a_{II,\sigma}^r) \right) \times \left(\sum_{\sigma',r'} (a_{I,\sigma'}^{r',\dagger} a_{I,\sigma'}^{r'} + 2a_{III,\sigma'}^{r',\dagger} a_{III,\sigma'}^{r'}) \right), \quad (\text{A8a})$$

while in the exchange term,

$$H_{\tilde{U}}^{(X)} = -\frac{\tilde{U}}{8} \int dx \sum_{\sigma,\sigma'} \left(\sum_r r a_{I,\sigma}^{r,\dagger} a_{I,\sigma'}^r \right) \left(\sum_{r'} r' a_{I,\sigma'}^{r',\dagger} a_{I,\sigma}^{r'} \right). \quad (\text{A8b})$$

In the Cooper channel

$$H_{\tilde{U}}^{(C)} = -\frac{\tilde{U}}{8} \int dx \sum_{\sigma,\sigma'} \left(\sum_r r a_{I,\sigma}^{r,\dagger} a_{I,\sigma'}^{-r,\dagger} \right) \left(\sum_{r'} r' a_{I,\sigma'}^{r',\dagger} a_{I,\sigma}^{-r'} \right) \quad (\text{A8c})$$

only operators from the Fermipoint k_I are involved.

c. Hund's coupling. The treatment of Hund's coupling is analogous to the treatment of the interorbital Hubbard interaction.

In the density channel we obtain

$$H_J^{(0)} = -\frac{J}{8} \int dx \left(\sum_r (a_{I}^{r,\dagger} \bar{\sigma} a_I^r + 2a_{II}^{r,\dagger} \bar{\sigma} a_{II}^r) \right) \times \left(\sum_{r'} (a_{I}^{r',\dagger} \bar{\sigma} a_{I}^{r'} + 2a_{III}^{r',\dagger} \bar{\sigma} a_{III}^{r'}) \right), \quad (\text{A9a})$$

while in the exchange,

$$H_J^{(X)} = \frac{J}{8} \int dx \sum_{\sigma,\sigma'} \left(\sum_r r \bar{\sigma} a_I^r a_{I'}^{r,\dagger} \right)_{\sigma\sigma'} \times \left(\sum_{r'} r' \bar{\sigma} a_{I'}^{r',\dagger} a_I^{r'} \right)_{\sigma',\sigma} \quad (\text{A9b})$$

and Cooper channel,

$$H_J^{(C)} = \frac{J}{8} \int dx \sum_{\sigma,\sigma'} \sum_{\bar{\sigma},\bar{\sigma}'} (\bar{\sigma}^T)_{\sigma,\bar{\sigma}} (\bar{\sigma}')_{\sigma',\bar{\sigma}'} \left(\sum_r r a_{I,\bar{\sigma}}^{r,\dagger} a_{I,\bar{\sigma}'}^{-r,\dagger} \right) \times \left(\sum_{r'} r' a_{I,\bar{\sigma}'}^{r',\dagger} a_{I,\bar{\sigma}}^{-r'} \right). \quad (\text{A9c})$$

only operators from the Fermipoint k_I are involved.

At $U = \tilde{U}$, the interaction terms presented in this Appendix may be rearranged in the form of scalar and vector current densities and ultimately yield Eq. (11) of the main text. In contrast, if $\tilde{U} = U - \tilde{J}$ additions to the

coupling constants with the following form arise

$$\delta \tilde{f}_{\alpha\beta}^\rho = -\frac{\tilde{J}}{4} \begin{pmatrix} 0 & 1 & 1 \\ 1 & 0 & 2 \\ 1 & 2 & 0 \end{pmatrix}_{\alpha\beta}, \quad (\text{A10a})$$

$$\delta \tilde{f}_{\alpha\beta}^\sigma = 0, \quad (\text{A10b})$$

$$\delta \tilde{c}_{\alpha\beta}^\rho = -\frac{\tilde{J}}{4} \begin{pmatrix} 3 & 0 & 0 \\ 0 & 0 & 0 \\ 0 & 0 & 0 \end{pmatrix}_{\alpha\beta}, \quad (\text{A10c})$$

$$\delta \tilde{c}_{\alpha\beta}^\sigma = \tilde{J} \begin{pmatrix} 1 & 0 & 0 \\ 0 & 0 & 0 \\ 0 & 0 & 0 \end{pmatrix}_{\alpha\beta}. \quad (\text{A10d})$$

Appendix B: RG flow - incommensurate filling

In this appendix we collect representative numerical solutions of the RG equations for each of the four phases presented in Fig. 2 of the main text. We also present some technical details from the analysis of the phases, beginning with the $\tilde{J} = 0$ phases, in increasing order of J/U . In Fig. 7 we show the phase diagram obtained for a different set of Fermi velocities to those used in Fig. 2, showing how the phase boundaries shift with velocities. We have left the discussion of finite \tilde{J} for appendix B 5

1. RG equations

The RG equations for an N-leg ladder without umklapp scattering were derived in Ref. [20]

$$\dot{f}_{\alpha\beta}^\rho = (c_{\alpha\beta}^\rho)^2 + \frac{3}{16} (c_{\alpha\beta}^\sigma)^2, \quad (\text{B1a})$$

$$\dot{f}_{\alpha\beta}^\sigma = -(f_{\alpha\beta}^\sigma)^2 + 2c_{\alpha\beta}^\rho c_{\alpha\beta}^\sigma - \frac{1}{2} (c_{\alpha\beta}^\sigma)^2, \quad (\text{B1b})$$

$$\dot{c}_{\alpha\beta}^\rho = -\sum_\gamma \{ \alpha_{\alpha\beta,\gamma} (c_{\alpha\gamma}^\rho c_{\gamma\beta}^\rho + \frac{3}{16} c_{\alpha\gamma}^\sigma c_{\gamma\beta}^\sigma) \}, \quad (\text{B1c})$$

$$+ (c_{\alpha\beta}^\rho h_{\alpha\beta}^\rho + \frac{3}{16} c_{\alpha\beta}^\sigma h_{\alpha\beta}^\sigma)$$

$$\dot{c}_{\alpha\beta}^\sigma = -\sum_\gamma \{ \alpha_{\alpha\beta,\gamma} (c_{\alpha\gamma}^\rho c_{\gamma\beta}^\sigma + c_{\alpha\gamma}^\sigma c_{\gamma\beta}^\rho + \frac{1}{2} c_{\alpha\gamma}^\sigma c_{\gamma\beta}^\sigma) \}, \quad (\text{B1d})$$

$$+ (c_{\alpha\beta}^\rho h_{\alpha\beta}^\sigma + c_{\alpha\beta}^\sigma h_{\alpha\beta}^\rho - \frac{1}{2} c_{\alpha\beta}^\sigma h_{\alpha\beta}^\sigma)$$

Parameters without the tilde are defined by $f_{\alpha\beta}^\rho = \tilde{f}_{\alpha\beta}^\rho / \pi (v_\alpha + v_\beta)$ etc., the ratio $\alpha_{\alpha\beta,\gamma} = (v_\alpha + v_\gamma)(v_\beta + v_\gamma) / [2v_\gamma(v_\alpha + v_\beta)]$ and $h_{\alpha\beta}^{\rho,\sigma} = 2f_{\alpha\beta}^{\rho,\sigma} + \delta_{\alpha\beta} c_{\alpha\beta}^{\rho,\sigma}$. The dot indicates the derivative with respect to the running scale, $\dot{c} = dc/d\ln(L/\tilde{a})$, where \tilde{a} is the UV length scale.

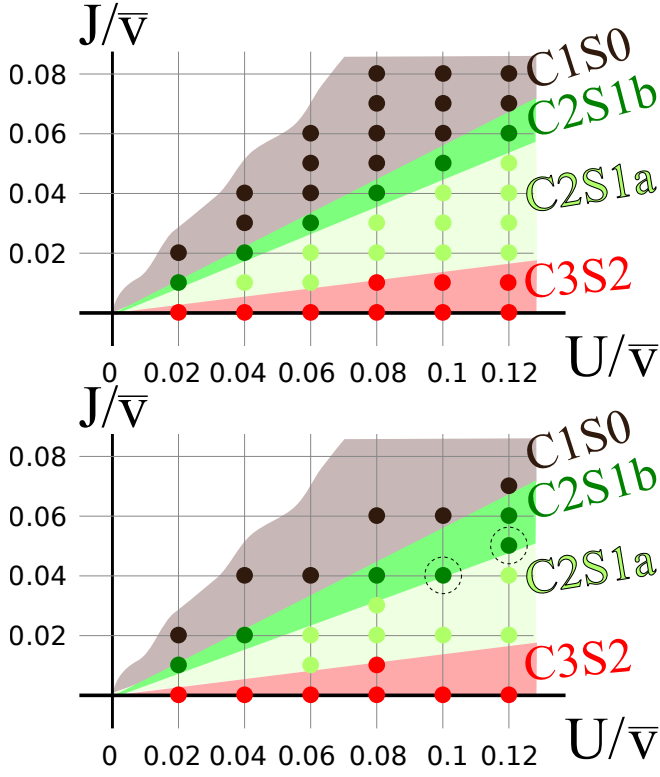


FIG. 7. Phase diagram for small Hubbard U and Hund's $J \leq U$, for the set of Fermi velocities used in Fig. 4 (top) and $v_I = v_{II} = 0.8eV$, $v_{III} = 0.6eV$ (bottom). In the second case, the system at $U = 0.1\bar{v}$, $J = 0.04\bar{v}$ and $U = 0.12\bar{v}$, $J = 0.05\bar{v}$ flows to the phase C2S1b (dashed circles), thus the boundary between C2S1b and C2S1a is shifted downwards.

2. Relationship $T_c(U)$

Here, we derive Eq. (13) of the main text. It is useful to employ the schematic representation Eq. (1) of the RG equations. If the coupling constants $g_\mu(y)$ obey the RG equations, so do $\bar{g}_\mu(y) = g_\mu(y/U)/U$. Let g_μ have an instability at $y_c(g_\mu^0)$, where $y_c(g_\mu^0)$ is an unknown function of the bare values g_μ^0 . Clearly, the instability of \bar{g}_μ occurs at $y_c(g_\mu^0/U)$ and in view of the relationship between $g_\mu(y)$ and $\bar{g}_\mu(y)$ it follows that

$$y_c(g_\mu^0/U) = U y_c(g_\mu^0). \quad (\text{B2})$$

Using $y_c = \ln(\Lambda/T_c)$ Eq. (13) of the main text follows.

3. Analysis of RG flow

a. C3S2 phase The phase of smallest J/U is characterized by the lone divergence of $c_{I,I}^\sigma \rightarrow -\infty$, while all other coupling constants remain featureless (see Fig. 8). Expanding the set of RG equations in powers of $c_{I,I}^\sigma$ one we confirm that the flow of $c_{I,I}^\sigma$ decouples from all other RG equations and diverges as $\dot{c}_{I,I}^\sigma = -(c_{I,I}^\sigma)^2$.

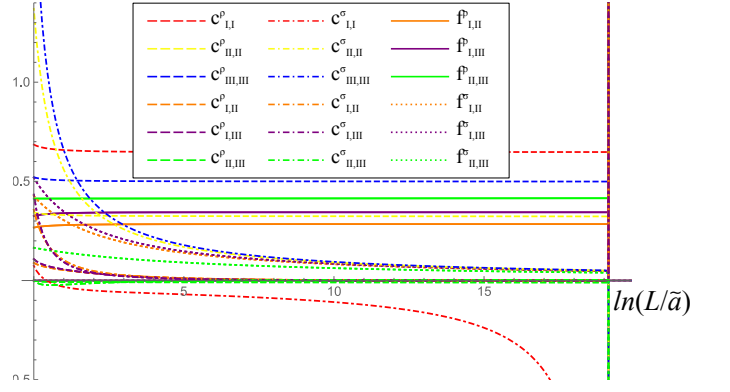


FIG. 8. Numerical integration of RG equations for starting values determined by $U/\bar{v} = 5$ and $J/U = 0.1$. In this case, the system flows to the C3S2 phase, which is characterized by divergent $c_{I,I}^\sigma$.

b. C2S1a phase. The phase of second smallest J/U , plotted in light green in Fig. 2, is characterized by a divergence of several coupling constants, while the ratio to $c_{II,III}^\sigma \rightarrow +\infty$ is fixed throughout the phase

$$c_{II,II}^\rho = c_{III,III}^\rho = -\frac{R_1}{8} c_{II,III}^\sigma \quad (\text{B3a})$$

$$c_{II,III}^\rho = -\frac{1}{4} c_{II,III}^\sigma \quad (\text{B3b})$$

$$f_{II,III}^\rho = \frac{1}{8} R_2 c_{II,III}^\sigma \quad (\text{B3c})$$

$$f_{II,III}^\sigma = -R_3 c_{II,III}^\sigma. \quad (\text{B3d})$$

The intraband, spin-spin interactions are equal and have a subdominant divergence $c_{II,II}^\sigma = c_{III,III}^\sigma \rightarrow +\infty$ but are small in comparison to the coupling constants of Eq. (B3), i.e. $c_{II,II}^\sigma/c_{II,III}^\sigma \rightarrow 0$. All other coupling constants remain small (see Fig. 9). The ansatz (B3), when introduced into the full RG equations, proves to be consistent provided ($\zeta = 1/2 + v_{II}/[4v_{III}] + v_{III}/[4v_{II}]$ is non-universal)

$$R_1 = \zeta R_2 \quad (\text{B4a})$$

$$R_2 = \frac{2R_3}{R_3^2 + 1} \quad (\text{B4b})$$

$$R_3 = \sqrt{\sqrt{\frac{8 + \zeta^2}{4}} - \frac{\zeta}{2}} \quad (\text{B4c})$$

For $v_{II} \rightarrow v_{III}$ all $R_{1,2,3}$ approach unity. The set of RG equations reduces to a single equation for one of the six parameters, $\dot{c}_{II,III}^\sigma = 2(c_{II,III}^\sigma)^2/R_2$.

c. C2S1b phase. The C2S1b phase is characterized by the following diverging running coupling constants where the sign of $c_{II,III}^\sigma \rightarrow -\infty$ constitutes the key differ-

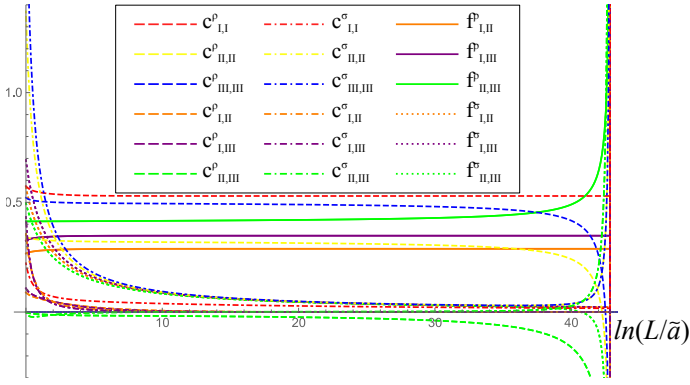


FIG. 9. Numerical integration of RG equations for starting values determined by $U/\bar{v} = 5$ and $J/U = 0.3$. In this case, the system flows to the C2S1a phase.

ence with the phase previously discussed.

$$c_{\text{II,II}}^{\rho} = c_{\text{III,III}}^{\rho} = \frac{R_1}{8} c_{\text{II,III}}^{\sigma} \quad (\text{B5a})$$

$$c_{\text{II,II}}^{\sigma} = c_{\text{III,III}}^{\sigma} = R_2 c_{\text{II,III}}^{\sigma} \quad (\text{B5b})$$

$$c_{\text{II,III}}^{\rho} = \frac{1}{4} c_{\text{II,III}}^{\sigma} \quad (\text{B5c})$$

$$f_{\text{II,III}}^{\rho} = -\frac{R_3}{8} c_{\text{II,III}}^{\sigma}. \quad (\text{B5d})$$

Though the coupling constants $f_{\text{II,III}}^{\sigma}$, increase near criticality, they remain relatively small $f_{\text{II,III}}^{\sigma}/c_{\text{II,III}}^{\sigma} \rightarrow 0$. Again, the ratios $R_{1,2,3}$ are constant throughout the phase and given in terms of α by the following functions which approach unity as $\zeta \rightarrow 1$.

$$R_1 = \zeta R_3 \quad (\text{B6a})$$

$$R_2 = \sqrt{\sqrt{\frac{8\zeta^2 + 1}{4}} - \frac{1}{2}} \quad (\text{B6b})$$

$$R_3 = \frac{2R_2}{R_2^2 + \zeta} \quad (\text{B6c})$$

The coupled divergences are captured by the single RG equation $\dot{c}_{\text{II,III}}^{\sigma} = -2(c_{\text{II,III}}^{\sigma})^2/R_3$.

d. C1S0 phase Finally, at the largest J we considered, coupling constants involving any of the three Fermi points diverge. As in the C2S1b phase and in Ref. [20], the ratio $c_{\alpha\beta}^{\rho} = c_{\alpha\beta}^{\sigma}/4$ for $\alpha \neq \beta$ is preserved and $f_{\alpha\beta}^{\sigma} \rightarrow 0$. In contrast with the previous discussion, the divergence of the intra Fermi point couplings $c_{\alpha\alpha}$ is generically i dependent. The sign of the diverging cou-

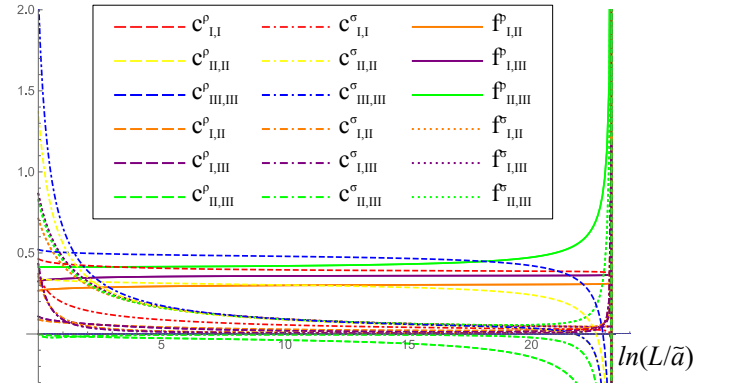


FIG. 10. Numerical integration of RG equations for starting values determined by $U/\bar{v} = 5$ and $J/U = 0.5$. In this case, the system flows to the C2S1b phase. Note that, as compared to Fig. 9, $c_{\text{II,III}}^{\sigma}$ flows towards negative infinity.

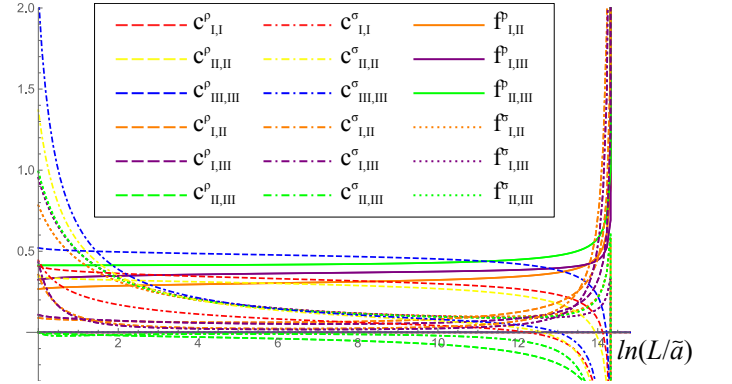


FIG. 11. Numerical integration of RG equations for starting values determined by $U/\bar{v} = 5$ and $J/U = 0.6$. In this case, the system flows to the C1S0 phase.

pling constants is

$$c_{\alpha\alpha}^{\sigma} \rightarrow -\infty \quad (\text{B7a})$$

$$c_{\alpha\alpha}^{\rho} \rightarrow -\infty \quad (\text{B7b})$$

$$c_{\text{I,II}}^{\sigma} = 4c_{\text{I,II}}^{\rho} \rightarrow +\infty \quad (\text{B7c})$$

$$c_{\text{II,III}}^{\sigma} = 4c_{\text{II,III}}^{\rho} \rightarrow -\infty \quad (\text{B7d})$$

$$c_{\text{I,III}}^{\sigma} = 4c_{\text{I,III}}^{\rho} \rightarrow +\infty \quad (\text{B7e})$$

$$f_{\alpha\beta}^{\rho} \rightarrow +\infty \quad (\text{B7f})$$

Once again, $f_{\alpha\beta}^{\sigma} > 0$ is small as compared to the couplings discussed in Eq. (B7) and formally $f_{\alpha\beta}^{\sigma} \rightarrow 0$ at the fixed point.

4. Physical meaning of the different phases

In the previous section we analyzed the RG flow and distinguished four different phases, characterized by the divergence of four different sets of coupling constants at a critical, exponentially large length scale L_* . Here, we study the physical implications of these four cases. In

this analysis we follow Ref. [20] and bosonize the theory near L_* subsequently using a semiclassical analysis.

a. Bosonization Dictionary

For the bosonization we use the dictionary

$$a_{\alpha,\sigma}^r(x) = \frac{1}{\sqrt{2\pi a}} \eta_{\alpha\sigma} e^{i\sqrt{4\pi}\phi_{\alpha,\sigma}^r(x)} \quad (\text{B8a})$$

with the following identities

$$\{\eta_{\alpha,\sigma}, \eta_{\alpha',\sigma'}\} = 2\delta_{\alpha\alpha'}\delta_{\sigma,\sigma'} \quad (\text{B8b})$$

$$\begin{aligned} \left[\phi_{\alpha,\sigma}^r(x), \phi_{\alpha',\sigma'}^{r'}(x') \right] &= \frac{ir}{4} \text{sign}(x-x') \delta_{rr'} \delta_{\alpha\alpha'} \delta_{\sigma,\sigma'} \\ &+ \frac{ir}{4} \delta_{r,-r'} \delta_{\alpha\alpha'} \delta_{\sigma,\sigma'}. \end{aligned} \quad (\text{B8c})$$

The length scale a_* is the UV cut-off of the renormalized theory. Since we have assumed the same Majorana Klein factor for creation and annihilation operators, normal ordering must be imposed prior to bosonization in order to preserve the consistency of signs. We assume that any operator under consideration contains an even number of fermionic operators from each Fermipoint β . Thus, in the Klein factor Hilbert space, each operator involving Fermi point β contains one of the following 4 operators at least once:

$$\eta_{\beta,\uparrow}\eta_{\beta,\uparrow} = 1; \eta_{\beta,\downarrow}\eta_{\beta,\downarrow} = 1; \eta_{\beta,\uparrow}\eta_{\beta,\downarrow} \equiv g_\beta; \eta_{\beta,\downarrow}\eta_{\beta,\uparrow} \equiv -g_\beta. \quad (\text{B9})$$

The algebra of g_β is $g_\beta^2 = -1$ and $[g_\gamma, g_\beta] = 0$, a representation of this algebra is

$$g_\beta = i, \quad \forall j. \quad (\text{B10})$$

We introduce density and displacement fields

$$\phi_{\alpha,\sigma}^R = \frac{\Phi_{\alpha,\sigma} + \Theta_{\alpha,\sigma}}{2}, \quad (\text{B11})$$

$$\phi_{\alpha,\sigma}^L = \frac{\Phi_{\alpha,\sigma} - \Theta_{\alpha,\sigma}}{2}. \quad (\text{B12})$$

Spin charge separation is accounted for by the parametrization

$$\Phi_\alpha^\rho = \frac{\Phi_{\alpha,\uparrow} + \Phi_{\alpha,\downarrow}}{\sqrt{2}} \quad (\text{B13})$$

$$\Phi_\alpha^s = \frac{\Phi_{\alpha,\uparrow} - \Phi_{\alpha,\downarrow}}{\sqrt{2}} \quad (\text{B14})$$

and analogously for Θ variables. Using our bosonization convention, Φ_α^ρ turns out to be proportional to the collective phase for a superconducting ground state.

b. Operators under consideration.

The phases under consideration are of the superconducting and charge density wave (CDW) /spin density wave (SDW) type. We study correlation functions of CDW, SDW_z (z -component of the SDW order parameter), singlet superconductivity (SS) and the z -component of triplet superconductivity (TS_z). The phases under consideration regard the following intraband operators,

$$\begin{aligned} O_{\text{CDW}}^{(\alpha)} &= (a_{\alpha,\uparrow}^{R,\dagger} a_{\alpha,\uparrow}^L + a_{\alpha,\downarrow}^{R,\dagger} a_{\alpha,\downarrow}^L) e^{-i2k_\alpha x} \\ &\sim \frac{1}{(\pi a)} e^{-i\sqrt{2\pi}\Theta_\alpha^\rho} \cos(\sqrt{2\pi}\Theta_\alpha^s) e^{-i2k_\alpha x}, \end{aligned} \quad (\text{B15a})$$

$$\begin{aligned} O_{\text{SDW}_z}^{(\alpha)} &= (a_{\alpha,\uparrow}^{R,\dagger} a_{\alpha,\uparrow}^L - a_{\alpha,\downarrow}^{R,\dagger} a_{\alpha,\downarrow}^L) e^{-i2k_\alpha x} \\ &\sim \frac{1}{(\pi a)} e^{-i\sqrt{2\pi}\Theta_\alpha^\rho} \sin(\sqrt{2\pi}\Theta_\alpha^s) e^{-i2k_\alpha x}, \end{aligned} \quad (\text{B15b})$$

$$\begin{aligned} O_{\text{SS}}^{(\alpha)} &= (a_{\alpha,\uparrow}^{R,\dagger} a_{\alpha,\downarrow}^{L,\dagger} - a_{\alpha,\downarrow}^{R,\dagger} a_{\alpha,\uparrow}^{L,\dagger}) \\ &\sim \frac{1}{(\pi a)} e^{-i\sqrt{2\pi}\Phi_\alpha^\rho} \cos(\sqrt{2\pi}\Theta_\alpha^s), \end{aligned} \quad (\text{B15c})$$

$$\begin{aligned} O_{\text{TS}_z}^{(\alpha)} &= (a_{\alpha,\uparrow}^{R,\dagger} a_{\alpha,\downarrow}^{L,\dagger} + a_{\alpha,\downarrow}^{R,\dagger} a_{\alpha,\uparrow}^{L,\dagger}) \\ &\sim \frac{1}{(\pi a)} e^{-i\sqrt{2\pi}\Phi_\alpha^\rho} \sin(\sqrt{2\pi}\Theta_\alpha^s), \end{aligned} \quad (\text{B15d})$$

as well as the following interband operators in the particle-hole channels

$$O_{CDW}^{(\alpha\beta)} = \frac{1}{2}(a_{\alpha,\uparrow}^{R,\dagger}a_{\beta,\uparrow}^L + a_{\alpha,\downarrow}^{R,\dagger}a_{\beta,\downarrow}^L)e^{-i(k_\alpha+k_\beta)x} + \alpha \leftrightarrow \beta$$

$$\sim e^{-i(k_\alpha+k_\beta)x} \frac{e^{-i\sqrt{\pi}\Theta_{\alpha\beta}^{\rho+}}}{\pi a} \left(\cos(\sqrt{\pi}\Phi_{\alpha\beta}^{\rho-}) \cos(\sqrt{\pi}\Theta_{\alpha\beta}^{s+}) \sin(\sqrt{\pi}\Phi_{\alpha\beta}^{s-}) - i \sin(\sqrt{\pi}\Phi_{\alpha\beta}^{\rho-}) \sin(\sqrt{\pi}\Theta_{\alpha\beta}^{s+}) \cos(\sqrt{\pi}\Phi_{\alpha\beta}^{s-}) \right) \quad (\text{B15e})$$

$$O_{SDW_z}^{(\alpha\beta)} = \frac{1}{2}(a_{\alpha,\uparrow}^{R,\dagger}a_{\beta,\uparrow}^L - a_{\alpha,\downarrow}^{R,\dagger}a_{\beta,\downarrow}^L)e^{-i(k_\alpha+k_\beta)x} + \alpha \leftrightarrow \beta$$

$$\sim e^{-i(k_\alpha+k_\beta)x} \frac{e^{-i\sqrt{\pi}\Theta_{\alpha\beta}^{\rho+}}}{\pi a} \left(\cos(\sqrt{\pi}\Phi_{\alpha\beta}^{\rho-}) \sin(\sqrt{\pi}\Theta_{\alpha\beta}^{s+}) \sin(\sqrt{\pi}\Phi_{\alpha\beta}^{s-}) - i \sin(\sqrt{\pi}\Phi_{\alpha\beta}^{\rho-}) \cos(\sqrt{\pi}\Theta_{\alpha\beta}^{s+}) \cos(\sqrt{\pi}\Phi_{\alpha\beta}^{s-}) \right) \quad (\text{B15f})$$

$$O_{CDW}^{[\alpha\beta]} = \frac{1}{2}(a_{\alpha,\uparrow}^{R,\dagger}a_{\beta,\uparrow}^L + a_{\alpha,\downarrow}^{R,\dagger}a_{\beta,\downarrow}^L)e^{-i(k_\alpha+k_\beta)x} - \alpha \leftrightarrow \beta$$

$$\sim e^{-i(k_\alpha+k_\beta)x} \frac{e^{-i\sqrt{\pi}\Theta_{\alpha\beta}^{\rho+}}}{\pi a} \left(\cos(\sqrt{\pi}\Phi_{\alpha\beta}^{\rho-}) \sin(\sqrt{\pi}\Theta_{\alpha\beta}^{s+}) \cos(\sqrt{\pi}\Phi_{\alpha\beta}^{s-}) - i \sin(\sqrt{\pi}\Phi_{\alpha\beta}^{\rho-}) \cos(\sqrt{\pi}\Theta_{\alpha\beta}^{s+}) \sin(\sqrt{\pi}\Phi_{\alpha\beta}^{s-}) \right) \quad (\text{B15g})$$

$$O_{SDW_z}^{[\alpha\beta]} = \frac{1}{2}(a_{\alpha,\uparrow}^{R,\dagger}a_{\beta,\uparrow}^L - a_{\alpha,\downarrow}^{R,\dagger}a_{\beta,\downarrow}^L)e^{-i(k_\alpha+k_\beta)x} - \alpha \leftrightarrow \beta$$

$$\sim e^{-i(k_\alpha+k_\beta)x} \frac{e^{-i\sqrt{\pi}\Theta_{\alpha\beta}^{\rho+}}}{\pi a} \left(\cos(\sqrt{\pi}\Phi_{\alpha\beta}^{\rho-}) \cos(\sqrt{\pi}\Theta_{\alpha\beta}^{s+}) \cos(\sqrt{\pi}\Phi_{\alpha\beta}^{s-}) - i \sin(\sqrt{\pi}\Phi_{\alpha\beta}^{\rho-}) \sin(\sqrt{\pi}\Theta_{\alpha\beta}^{s+}) \sin(\sqrt{\pi}\Phi_{\alpha\beta}^{s-}) \right). \quad (\text{B15h})$$

c. Interactions

For the purposes of classifying the instabilities presented in Figs. 8-11, it is sufficient to keep only those interactions which generate potential terms (e.g. cosine terms) of bosonic fields

$$\mathcal{H}_{\text{int}} = - \sum_{\alpha\beta} \frac{\tilde{f}_{\alpha\beta}^\sigma}{2} \sum_{\sigma} a_{\alpha,\sigma}^{R,\dagger} a_{\beta,\bar{\sigma}}^{L,\dagger} a_{\beta,\sigma}^L a_{\alpha,\bar{\sigma}}^R$$

$$+ \sum_{\alpha \neq \beta} \sum_{\sigma, \sigma'} \left(\tilde{c}_{\alpha\beta}^\rho + \frac{\tilde{c}_{\alpha\beta}^\sigma}{4} \right) a_{\alpha,\sigma}^{R,\dagger} a_{\alpha,\sigma'}^{L,\dagger} a_{\beta,\sigma'}^L a_{\beta,\sigma}^R$$

$$- \sum_{(\alpha,\sigma) \neq (\beta,\sigma')} \frac{\tilde{c}_{\alpha\beta}^\sigma}{2} a_{\alpha,\sigma}^{R,\dagger} a_{\alpha,\sigma'}^{L,\dagger} a_{\beta,\sigma}^L a_{\beta,\sigma'}^R, \quad (\text{B16})$$

where from now on $\tilde{c}_{\alpha\beta}^\sigma$ etc. are to be understood as the renormalized coupling constants. The notation $\bar{\sigma}$ means \downarrow (\uparrow) for $\sigma = \uparrow$ ($\sigma = \downarrow$). A bosonization of these terms is presented for each phase separately.

In addition, interactions can generate gradient terms of bosons

$$\mathcal{H}_{\nabla^2} = \frac{(v_\alpha + v_\beta)C_{\alpha\beta}^\rho}{2} \left[\nabla\Theta_\alpha^\rho \nabla\Theta_\beta^\rho - \nabla\Phi_\alpha^\rho \nabla\Phi_\beta^\rho \right]$$

$$+ \frac{(v_\alpha + v_\beta)C_{\alpha\beta}^\sigma}{8} \left[\nabla\Phi_\alpha^s \nabla\Phi_\beta^s - \nabla\Theta_\alpha^s \nabla\Theta_\beta^s \right] \quad (\text{B17a})$$

with

$$C_{\alpha\beta}^{\rho,\sigma} = \begin{pmatrix} c_{I,I}^{\rho,\sigma} & f_{I,II}^{\rho,\sigma} & f_{I,III}^{\rho,\sigma} \\ f_{I,II}^{\rho,\sigma} & c_{II,II}^{\rho,\sigma} & f_{II,III}^{\rho,\sigma} \\ f_{I,III}^{\rho,\sigma} & f_{II,III}^{\rho,\sigma} & c_{III,III}^{\rho,\sigma} \end{pmatrix}_{\alpha\beta}. \quad (\text{B17b})$$

For the RG procedure it is useful to express the contractions of fast fields in terms of a Luttinger parameter matrix

$$\left\langle \Theta_\alpha^{\rho,s} \Theta_\beta^{\rho,s} \right\rangle_{\text{fast}} = \frac{1}{2\pi} \ln(L/a^*) \underline{K}_{\alpha\beta}^{\rho,\sigma} \quad (\text{B18})$$

$$\left\langle \Phi_\alpha^{\rho,s} \Phi_\beta^{\rho,s} \right\rangle_{\text{fast}} = \frac{1}{2\pi} \ln(L/a^*) [(\underline{K}^{\rho,\sigma})^{-1}]_{\alpha\beta} \quad (\text{B19})$$

where L is running length scale.

$$\underline{K}_{\alpha\beta}^\rho \simeq \delta_{\alpha\beta} - 2C_{\alpha\beta}^\rho, \quad (\text{B20a})$$

$$\underline{K}_{\alpha\beta}^\sigma \simeq \delta_{\alpha\beta} + C_{\alpha\beta}^\sigma/2. \quad (\text{B20b})$$

d. Phases under consideration

We now investigate each of the four phases obtained from the RG analysis.

a. C3S2 phase. The potential part of the bosonized Hamiltonian in the C3S2 phase is

$$\mathcal{H}_{\text{int}} \sim \frac{1}{(2\pi a^*)^2} c_{I,I}^\sigma \cos(\sqrt{8\pi}\Theta_{I,s}). \quad (\text{B21})$$

Since $c_{I,I}^\sigma < 0$, the system locks into one of the minima $\sqrt{2/\pi}\Theta_I^s \in \mathbb{Z}$ and thus only two out of three spin modes remain gapless. Comparing with Eqs. (B15), we readily see that $O_{CDW}^{(I)}$ and $O_{SS}^{(I)}$ have algebraic correlations, while SDW and TS correlations are massive. Fermions near $k_{II,III}$ remain unaffected of the condensation of Θ_I^s .

b. C2S1a phase. Using Eqs. (B3), Eq. (B16) becomes

$$\begin{aligned} \mathcal{H}_{\text{int}} = & -\frac{1}{2} \sum_{\alpha \neq \beta} \left\{ \sum_{\sigma} \tilde{f}_{\alpha\beta}^{\sigma} a_{\alpha,\sigma}^{R,\dagger} a_{\alpha,\sigma}^{L,\dagger} a_{\beta,\sigma}^{L} a_{\beta,\sigma}^{R} \right. \\ & \left. + \sum_{\sigma,\sigma'} \tilde{c}_{\alpha\beta}^{\sigma} a_{\alpha,\sigma}^{R,\dagger} a_{\alpha,\sigma'}^{L,\dagger} a_{\beta,\sigma}^{L} a_{\beta,\sigma'}^{R} \right\} \\ \sim & -\frac{1}{(2\pi a_*)^2} \sum_{\alpha \neq \beta} \left\{ \tilde{f}_{\alpha\beta}^{\sigma} \cos[2\sqrt{\pi}(\Phi_{\alpha\beta}^{s-} + \Theta_{\alpha\beta}^{s+})] \right. \\ & \left. + \tilde{c}_{\alpha\beta}^{\sigma} \cos(2\sqrt{\pi}\Phi_{\alpha\beta}^{\rho-}) \cos(2\sqrt{\pi}\Phi_{\alpha\beta}^{s-}) \right. \\ & \left. - \tilde{c}_{\alpha\beta}^{\sigma} \cos(2\sqrt{\pi}\Phi_{\alpha\beta}^{\rho-}) \cos(2\sqrt{\pi}\Theta_{\alpha\beta}^{s+}) \right\}. \quad (\text{B22}) \end{aligned}$$

Here we have introduced $\Phi_{\alpha\beta}^{\rho\pm} = (\Phi_{\alpha}^{\rho} \pm \Phi_{\beta}^{\rho})/\sqrt{2}$ and analogous notations for all other channels. Since $\tilde{f}_{\alpha\beta}^{\sigma} \rightarrow -\infty$ and $\tilde{c}_{\alpha\beta}^{\sigma} \rightarrow +\infty$, there are two sets of solutions which minimize the potential energy for $\alpha, \beta \in \{\text{II,III}\}; \alpha \neq \beta$

$$\Phi_{\alpha\beta}^{\rho-}/\sqrt{\pi} \in \mathbb{Z}, \quad \Phi_{\alpha\beta}^{s-}/\sqrt{\pi} \in \mathbb{Z}, \quad \Theta_{\alpha\beta}^{s+}/\sqrt{\pi} \in \mathbb{Z} + 1/2, \quad (\text{B23a})$$

$$\Phi_{\alpha\beta}^{\rho-}/\sqrt{\pi} \in \mathbb{Z} + 1/2, \quad \Phi_{\alpha\beta}^{s-}/\sqrt{\pi} \in \mathbb{Z} + 1/2, \quad \Theta_{\alpha\beta}^{s+}/\sqrt{\pi} \in \mathbb{Z}. \quad (\text{B23b})$$

The low energy theory perturbing about any of the given minima is the same for either solution. Fermions with momenta close to k_{I} remain unaffected. Only two charge and one spin mode remain gapless, hence the notation C2S1. Comparison with Eqs. (B15) demonstrates that for any of the two solutions of (B23) the operator $O_{CDW}^{[\text{II,III}]}$ orders. Note that, in view of the locking of $\Phi_{\alpha\beta}^{\rho-}$ into a minimum, the conjugate variable $\Theta_{\alpha\beta}^{\rho-}$ is maximally uncertain and thus $O_{SS}^{[\text{II,III}]}$ and $O_{TS_z}^{[\text{II,III}]}$ do not display long range correlations in either case.

It is instructive to refermionize the interaction term of excitations near Fermi points II,III in the basis of fermions describing fluctuations in the relative charge, relative spin and total spin sectors. Assuming $v_{\text{II}} = v_{\text{III}}$ for simplicity, Eq. (B22) may be written as

$$\mathcal{H}_{\text{int}} = -|\tilde{f}_{\text{II,III}}^{\sigma}| [M_{s-} - M_{s+} - M_{\rho-} - M_{s-} + M_{s+} M_{\rho-}], \quad (\text{B24})$$

where we introduce mass terms

$$M_a = a_a^{R,\dagger} a_a^L + a_a^{L,\dagger} a_a^R, \quad \text{with } a = \rho^-, s^-, s^+. \quad (\text{B25})$$

If we further perform a gauge transformation in the $(s, +)$ sector, $a_{s,+}^L \rightarrow -a_{s,+}^L$, Eq. (B24) corresponds to the interaction term of an $\text{SO}(6) \sim \text{SU}(4)$ Gross-Neveu model.

c. C2S1b and C1S0 phases. Again, we keep only the dominant coupling constants and exploit $c_{\alpha\beta}^{\rho} = c_{\alpha\beta}^{\sigma}/4$ for

$\alpha \neq \beta$. Then

$$\begin{aligned} \mathcal{H}_{\text{int}} = & -\sum_{\alpha,\sigma} \frac{\tilde{c}_{\alpha\alpha}^{\sigma}}{2} a_{\alpha,\sigma}^{R,\dagger} a_{\alpha,\sigma}^{L,\dagger} a_{\alpha,\sigma}^L a_{\alpha,\sigma}^R \\ & - \sum_{\alpha \neq \beta} \sum_{\sigma} \frac{\tilde{c}_{\alpha\beta}^{\sigma}}{2} a_{\alpha,\sigma}^{R,\dagger} a_{\alpha,\sigma}^{L,\dagger} (a_{\beta,\sigma}^L a_{\beta,\sigma}^R - a_{\beta,\sigma}^L a_{\beta,\sigma}^R) \\ \sim & \frac{1}{(2\pi a_*)^2} \left\{ \tilde{c}_{\alpha\alpha}^{\sigma} \cos(\sqrt{8\pi}\Theta_{\alpha}^s) \right. \\ & \left. + 4 \sum_{\alpha < \beta} \tilde{c}_{\alpha\beta}^{\sigma} \cos(\sqrt{4\pi}\Phi_{\alpha\beta}^{\rho-}) \cos(\sqrt{2\pi}\Theta_{\alpha}^s) \cos(\sqrt{2\pi}\Theta_{\beta}^s) \right\}. \quad (\text{B26}) \end{aligned}$$

We note that in the C2S1b phase, $\tilde{c}_{\alpha\beta}^{\sigma} \rightarrow -\infty$ for $\alpha, \beta = \text{II,III}$. Thus the minimum of the potential is

$$\sqrt{2/\pi}\Theta_{\text{II},s} \in \mathbb{Z}, \quad \sqrt{2/\pi}\Theta_{\text{III},s} \in \mathbb{Z}, \quad \Phi_{\text{II,III}}^{\rho-}/\sqrt{\pi} \in \mathbb{Z}. \quad (\text{B27})$$

Thus the C2S1b phase has two gapless charge modes and one gapless spin mode. It is, in essence, a spinful Luttinger liquid near Fermi point k_{I} and a superconductor with equal gaps ($\tilde{c}_{\text{II,II}}^{\sigma} = \tilde{c}_{\text{III,III}}^{\sigma}$) at Fermi points $k_{\text{II,III}}$. Again, we can refermionize the interaction term of the C2S1b phase in the same channels as in the case of C2S1a. At $v_{\text{II}} = v_{\text{III}}$ we obtain

$$\mathcal{H}_{\text{int}} = -2|\tilde{c}_{\text{II,II}}^{\sigma}| [M_{s+} M_{s-} + M_{\rho-} (M_{s+} + M_{s-})] \quad (\text{B28})$$

which represents an $\text{SO}(6)$ Gross-Neveu model, albeit in a different phase than in the case of C2S1a.

The C1S0 phase is characterized by $\tilde{c}_{\alpha\alpha}^{\sigma} \rightarrow -\infty$, $\tilde{c}_{\text{II,III}}^{\sigma} \rightarrow -\infty$ and $\tilde{c}_{\text{I,II}}^{\sigma} \rightarrow \infty$, $\tilde{c}_{\text{I,III}}^{\sigma} \rightarrow \infty$. Therefore, the minimum occurs at

$$\sqrt{2/\pi}\Theta_{\alpha,s} \in \mathbb{Z}, \quad \Phi_{\text{I,II}}^{\rho-}/\sqrt{\pi} \in \mathbb{Z} + 1/2, \quad (\text{B29})$$

$$\Phi_{\text{I,III}}^{\rho-}/\sqrt{\pi} \in \mathbb{Z} + 1/2, \quad \Phi_{\text{II,III}}^{\rho-}/\sqrt{\pi} \in \mathbb{Z}. \quad (\text{B30})$$

Since $\Phi_{\text{I,II}}^{\rho-} = \Phi_{\text{I,III}}^{\rho-} - \Phi_{\text{II,III}}^{\rho-}$ there are two independent constraints on bosons in the charge sector and three independent constraints on bosons in the spin sector, justifying the notation C1S0. This phase is a fully gapped spin singlet s_{+--} intraband superconductor with the following products of gap functions: $\Delta_{\text{I}}\Delta_{\text{II}} < 0, \Delta_{\text{I}}\Delta_{\text{III}} < 0, \Delta_{\text{II}}\Delta_{\text{III}} > 0$.

5. Unequal interorbital and intra-orbital repulsion

This appendix examines the effect of unequal inter and intra-orbital repulsion, i.e. $\tilde{J} \neq 0$ in Eqs. (11),(A10). We note that at $\tilde{J} = J$, the Hubbard-Kanamori interaction takes the form

$$\begin{aligned} H_U(j) = & \frac{U}{2} \sum_{\substack{\tau,\gamma,\sigma, \\ \gamma',\sigma'}}' n_{\tau\gamma\sigma}(j) n_{\tau\gamma'\sigma'}(j) \\ & + 2J \sum_{\tau} \{ [T_{\tau}^{(x)}(j)]^2 + [T_{\tau}^{(y)}(j)]^2 \}. \quad (\text{B31}) \end{aligned}$$

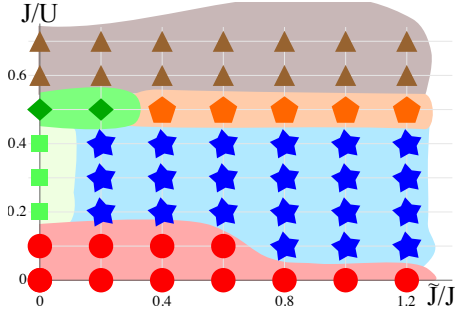


FIG. 12. Summary of the integration of RG equations at finite \tilde{J}/J and $U/\bar{v} = 5$. In addition to the phases C3S2 (red dots), C2S1a (light green squares), C2S1b (dark green diamonds), C1S0 (brown triangles) we find an additional phase C2S1c (orange pentagons). For all of those phases the divergence occurs at running scales $y_c < 100$ (for C1S0 and C3S2 $y_c < 27$) while in the extended critical region (blue stars), no divergence occurs for any $y \leq 1000$.

Here, $T_\tau^{(\mu)}(j) = d_{\sigma,\tau}^\dagger \tilde{\tau}_\mu d_{\sigma,\tau} / 2$ is the orbital isospin operator and $\tilde{\tau}_\mu$ are Pauli matrices in orbital space.

The integration of RG equations for general $0 \leq J/U \leq 0.7$ and $0 \leq \tilde{J}/J < 1.2$ reveals five phases and a rather extended critical regime (see Fig. 12). In addition to the four phases discussed in the main text there is an extended critical regime corresponding to the C3S3 QCP of Fig. 3 where the numerical integration of RG (consistently performed at $U = 5\bar{v}$) does not reveal a divergence for any $y < 1000$ (see Fig. 14). This corroborates the finding summarized in Fig. 3 and highlights the importance of the critical phase.

A typical RG flow for the phase C2S1c is shown in Fig. 13. Among the data points of Fig. 12 which fall into the C2S1c phase, $\tilde{J} = 1.2J, J = 0.5U$ has the highest $T_c \sim 0.1mK$ for $\Lambda = 1eV$ at $U/\bar{v} = 5$. This phase is characterized by $c_{I,I}^\sigma \simeq c_{I,I}^\sigma \simeq -4c_{I,II}^\rho \simeq -c_{I,II}^\sigma \rightarrow -\infty$ with $c_{I,I}^\rho \simeq c_{II,II}^\rho = -f_{I,II}^\rho \rightarrow -\infty$. We now can exploit Eq. (B26) for $\alpha, \beta \in \{I, II\}$, revealing that the minimum given by

$$\sqrt{2/\pi}\Theta_{I,s} \in \mathbb{Z}, \quad \sqrt{2/\pi}\Theta_{II,s} \in \mathbb{Z}, \quad \Phi_{I,II}^\rho / \sqrt{\pi} \in \mathbb{Z} + 1/2. \quad (\text{B32})$$

describes a two band superconductor with relative phase π .

Appendix C: Umklapp scattering

In this appendix we provide details on umklapp scattering as a discussed in Sec. IV.

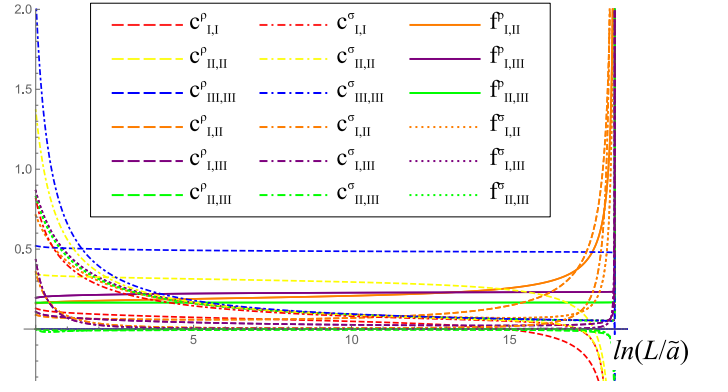


FIG. 13. Numerical integration of RG equations for starting values determined by $U/\bar{v} = 5$ and $J/U = 0.5$, $\tilde{J} = 1.2J$. In this case, the system flows to the C2S1c phase.

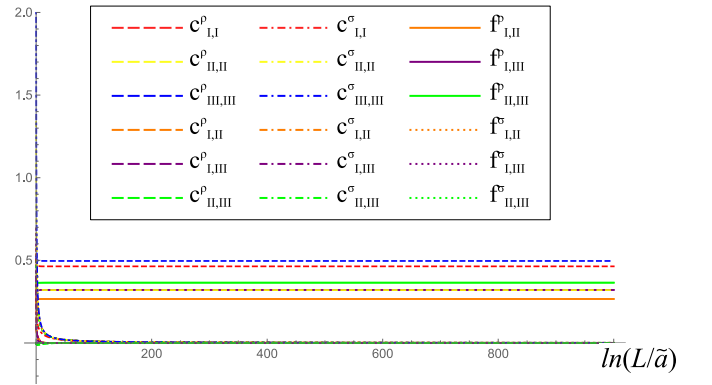


FIG. 14. Numerical integration of RG equations for starting values determined by $U/\bar{v} = 5$ and $J/U = 0.3$ and $\tilde{J} = 0.4J$. In this case, the system remains critical for any $y \leq 1000$.

1. Bosonization of umklapp terms

We consider

$$\mathcal{H}_u = -G_u(2\pi a) \left[\left(\prod_{\alpha=I}^{III} a_{\alpha,\sigma_\alpha}^{R,\dagger} a_{\alpha,\sigma_\alpha}^L \right) \delta_{\{\sigma'\},\{\sigma\}} \right] + H.c.. \quad (\text{C1})$$

The symbol $\delta_{\{\sigma'\},\{\sigma\}}$ implies equality of the two sets $\{\sigma'_I \sigma'_{II} \sigma'_{III}\}$ and $\{\sigma_I \sigma_{II} \sigma_{III}\}$ of spin indices, which reflects the overall spin conservation. Note that the spin is not conserved within any given pair of Fermi points, i.e. in general $\sigma_\alpha \neq \sigma'_\alpha$ (see Fig. 5). A summation over all permutations of spin indices which preserve the overall spin conservation is implied. For this section we therefore concentrate on the term which is fully symmetric under exchange of spin indices, more generic terms are discussed afterwards.

Bosonization of Eq. (C1) leads to

$$\mathcal{H}_u = g_u e^{-i\sqrt{2\pi} \sum_{\alpha=I}^{III} \Theta_\alpha^s} \times \prod_{\alpha=I}^{III} \left[\cos(\sqrt{2\pi}\Theta_\alpha^s) - i \sin(\sqrt{2\pi}\Phi_\alpha^s) \right] + H.c.. \quad (\text{C2})$$

In principle, $g_u = i2G_u/(\pi a)^2$ can have both real and imaginary parts. This leads to an overall of 16 umklapp terms, all of which may have different bare values in the case of spin dependent G_u . In addition, under RG, interband interaction generates additional terms.

2. Analysis of umklapp scattering

We first analyze umklapp scattering in the Luttinger phase prior to an instability, proceeding to each of the phases obtained above. Employing fermionic diagrams, Fig. 5, illustrates that the three-body umklapp scattering can not renormalize two-body interactions at weak coupling in the one-loop approximation. Therefore we can determine the scaling dimension d_u of the most dominant umklapp process without considering its backreaction on the other coupling constants.

a. Umklapp scattering in the Luttinger liquid phase
When $C_{\alpha\beta}^\sigma$ has predominantly positive entries and \underline{K}^σ has eigenvalues large than unity, the umklapp terms with the largest dimension involve Φ_α^s , so we disregard all terms with Θ_α^s . We introduce $\Theta_{\text{tot}}^\rho = [\sum_\alpha \Theta_\alpha^\rho]/\sqrt{3}$

$$\begin{aligned} \mathcal{H}_u &= \cos(\sqrt{6\pi}\Theta_{\text{tot}}^\rho) \times \\ &\times \left[g_{sss} \sin(\sqrt{2\pi}\Phi_1^s) \sin(\sqrt{2\pi}\Phi_{\text{II}}^s) \sin(\sqrt{2\pi}\Phi_{\text{III}}^s) \right. \\ &+ g_{ssc} \sin(\sqrt{2\pi}\Phi_1^s) \cos(\sqrt{2\pi}\Phi_{\text{II}}^s) \cos(\sqrt{2\pi}\Phi_{\text{III}}^s) \\ &+ g_{csc} \cos(\sqrt{2\pi}\Phi_1^s) \sin(\sqrt{2\pi}\Phi_{\text{II}}^s) \cos(\sqrt{2\pi}\Phi_{\text{III}}^s) \\ &\left. + g_{ccs} \cos(\sqrt{2\pi}\Phi_1^s) \cos(\sqrt{2\pi}\Phi_{\text{II}}^s) \sin(\sqrt{2\pi}\Phi_{\text{III}}^s) \right]. \end{aligned} \quad (\text{C3})$$

By contrast, when $C_{\alpha\beta}^\sigma$ has (predominantly) negative eigenvalues we disregard terms with Φ_α^s and keep

$$\begin{aligned} \mathcal{H}_{\bar{u}} &= \cos(\sqrt{6\pi}\Theta_{\text{tot}}^\rho) \times \\ &\times \left[\tilde{g}_{ccc} \cos(\sqrt{2\pi}\Theta_1^s) \cos(\sqrt{2\pi}\Theta_{\text{II}}^s) \cos(\sqrt{2\pi}\Theta_{\text{III}}^s) \right. \\ &+ \tilde{g}_{css} \cos(\sqrt{2\pi}\Theta_1^s) \sin(\sqrt{2\pi}\Theta_{\text{II}}^s) \sin(\sqrt{2\pi}\Theta_{\text{III}}^s) \\ &+ \tilde{g}_{scs} \sin(\sqrt{2\pi}\Theta_1^s) \cos(\sqrt{2\pi}\Theta_{\text{II}}^s) \sin(\sqrt{2\pi}\Theta_{\text{III}}^s) \\ &\left. + \tilde{g}_{ssc} \sin(\sqrt{2\pi}\Theta_1^s) \sin(\sqrt{2\pi}\Theta_{\text{II}}^s) \cos(\sqrt{2\pi}\Theta_{\text{III}}^s) \right]. \end{aligned} \quad (\text{C4})$$

In both cases, terms with $\cos(\sqrt{6\pi}\Theta_{\text{tot}}^\rho) \rightarrow \sin(\sqrt{6\pi}\Theta_{\text{tot}}^\rho)$ may also exist. They have the same scaling dimension as the cosine terms shown here.

The tree level RG equations are

$$\begin{pmatrix} g_{sss} \\ g_{ssc} \\ g_{csc} \\ g_{ccs} \end{pmatrix} = \left[2 - \frac{3K_{\text{tot}}^\rho + \sum_\alpha (\underline{K}^{\sigma,-1})_{\alpha\alpha}}{2} + \begin{pmatrix} 0 & (\underline{K}^{\sigma,-1})_{\text{II,III}} & (\underline{K}^{\sigma,-1})_{\text{I,III}} & (\underline{K}^{\sigma,-1})_{\text{I,II}} \\ (\underline{K}^{\sigma,-1})_{\text{II,III}} & 0 & -(\underline{K}^{\sigma,-1})_{\text{I,II}} & -(\underline{K}^{\sigma,-1})_{\text{I,III}} \\ (\underline{K}^{\sigma,-1})_{\text{I,III}} & -(\underline{K}^{\sigma,-1})_{\text{I,II}} & 0 & -(\underline{K}^{\sigma,-1})_{\text{II,III}} \\ (\underline{K}^{\sigma,-1})_{\text{I,II}} & -(\underline{K}^{\sigma,-1})_{\text{I,III}} & -(\underline{K}^{\sigma,-1})_{\text{II,III}} & 0 \end{pmatrix} \right] \begin{pmatrix} g_{sss} \\ g_{ssc} \\ g_{csc} \\ g_{ccs} \end{pmatrix} \quad (\text{C5})$$

$$\begin{pmatrix} \tilde{g}_{ccc} \\ \tilde{g}_{css} \\ \tilde{g}_{scs} \\ \tilde{g}_{ssc} \end{pmatrix} = \left[2 - \frac{3K_{\text{tot}}^\rho + \sum_\alpha (\underline{K}^\sigma)_{\alpha\alpha}}{2} + \begin{pmatrix} 0 & (\underline{K}^\sigma)_{\text{II,III}} & (\underline{K}^\sigma)_{\text{I,III}} & (\underline{K}^\sigma)_{\text{I,II}} \\ (\underline{K}^\sigma)_{\text{II,III}} & 0 & -(\underline{K}^\sigma)_{\text{I,II}} & -(\underline{K}^\sigma)_{\text{I,III}} \\ (\underline{K}^\sigma)_{\text{I,III}} & -(\underline{K}^\sigma)_{\text{I,II}} & 0 & -(\underline{K}^\sigma)_{\text{II,III}} \\ (\underline{K}^\sigma)_{\text{I,II}} & -(\underline{K}^\sigma)_{\text{I,III}} & -(\underline{K}^\sigma)_{\text{II,III}} & 0 \end{pmatrix} \right] \begin{pmatrix} \tilde{g}_{ccc} \\ \tilde{g}_{css} \\ \tilde{g}_{scs} \\ \tilde{g}_{ssc} \end{pmatrix} \quad (\text{C6})$$

At the bare level interactions in the spin sector are weak and repulsive $C_{\alpha\beta}^\sigma > 0$, renormalize downwards as the QCP is approached (see Fig. 3). The Luttinger parameter in the total charge sector is

$$K_{\text{tot}}^\rho = \frac{\sum_{\alpha\beta} \underline{K}_{\alpha\beta}^\rho}{3}. \quad (\text{C7})$$

The largest scaling dimension, which occurs in Eq. (C5), is typically negative and as $[\underline{K}^\sigma]_{\alpha\beta} \rightarrow \delta_{\alpha\beta}$ from above,

becomes $[1 - 3K_{\text{tot}}^\rho]/2$. Thus, a three band LL with weak interactions does not display Mott localization.

b. Umklapp scattering in the C3S2 phase. In the C3S2 phase, Θ_1^s condenses, while the Luttinger parameter in the sector of channels II, III remains positive and approximately $c_{\text{II,II}}^\sigma = c_{\text{III,III}}^\sigma = f_{\text{II,III}}^\sigma \ll 1$ reflecting the spin symmetry being enhanced at the interband level.

The dominant umklapp terms are

$$\begin{aligned} \mathcal{H}_u &= \cos(\sqrt{6\pi}\Theta_{\text{tot}}^\rho) \times \\ &\times \left[g_{cc} \cos(\sqrt{2\pi}\Phi_{\text{II}}^s) \cos(\sqrt{2\pi}\Phi_{\text{III}}^s) \right. \\ &\left. + g_{ss} \sin(\sqrt{2\pi}\Phi_{\text{II}}^s) \sin(\sqrt{2\pi}\Phi_{\text{III}}^s) \right]. \end{aligned} \quad (\text{C8})$$

In this phase, there are three other pairs of operators which have the same RG equations, namely

$$\begin{aligned} \begin{pmatrix} g_{cc} \\ g_{ss} \end{pmatrix} &= \left[2 - \frac{3K_{\text{tot}}^\rho + \sum_{\alpha,\text{II}}^{\text{III}} (\underline{K}^{\sigma,-1})_{\alpha\alpha}}{2} \right. \\ &\left. + \begin{pmatrix} 0 & (\underline{K}^{\sigma,-1})_{\text{II,III}} \\ (\underline{K}^{\sigma,-1})_{\text{II,III}} & 0 \end{pmatrix} \right] \begin{pmatrix} g_{cc} \\ g_{ss} \end{pmatrix} \end{aligned} \quad (\text{C9})$$

The dominant operator is obtained for $g_{cc} = g_{ss}$ and has scaling dimension $2 - \frac{3K_{\text{tot}}^\rho + \sum_{\alpha,\text{II}}^{\text{III}} (\underline{K}^{\sigma,-1})_{\alpha\alpha} - 2(\underline{K}^{\sigma,-1})_{\text{II,III}}}{2} \simeq 1 - \frac{3K_{\text{tot}}^\rho}{2}$. Therefore, the Mott transition occurs at $K_{\text{tot}}^\rho = 2/3$ which requires rather strong interactions.

c. Umklapp scattering and the phase C2S1a. In this phase the spin sector of channels II, III is fully gapped and $0 < c_{\text{I,I}}^\sigma \ll \bar{v}$. We therefore concentrate on an umklapp term for which there is spin conservation within Fermi surface I, i.e.

$$\mathcal{H}_u = g \cos(\sqrt{6\pi}\Theta_{\text{tot}}^\rho) \cos(\sqrt{2\pi}\Theta_{\text{I}}^s). \quad (\text{C10})$$

and the analogous term obtained by $\cos(\sqrt{6\pi}\Theta_{\text{tot}}^\rho) \rightarrow \sin(\sqrt{6\pi}\Theta_{\text{tot}}^\rho)$. The scaling dimension of these terms is $2 - 3K_{\text{tot}}^\rho/2 - K_{\text{I,I}}^\sigma/2$ and thus the transition occurs at

$$K_{\text{tot}}^\rho = \frac{2}{3} \left[2 - \frac{K_{\text{I,I}}^\sigma}{2} \right] \approx 1. \quad (\text{C11})$$

We observe that the ordering in the spin sector promotes a Mott transition in its vicinity and we expect $K_{\text{tot}}^\rho < 1$. When the Mott transition occurs, the total charge mode Θ_{tot}^ρ freezes, corresponding to an electrical charge insulator. At the same time Θ_{I}^s freezes. Taken together, the phase C2S1a becomes a phase C1S0a.

The long-range correlations of $\mathcal{O}_{\text{CDW}}^{\text{II,III}}$ of the C2S1a phase survive the Mott transition and additional long-range correlations of $\mathcal{O}_{\text{CDW}}^{\text{I,I}}$ appear.

d. Umklapp scattering and the phase C2S1b. The umklapp terms of relevance for the phase C2S1b are the also given by Eq. (C10) and the transition to a phase C1S0b again occurs at $K_{\text{tot}}^\rho \approx 1$. All superconducting correlations are killed by the ordering of Θ_{tot}^ρ , the only long range correlations occur for $\mathcal{O}_{\text{CDW}}^{\text{I,I}}$.

e. Umklapp scattering and the phase C1S0. In the phase C1S0 all spin modes are frozen and only the pair

$\Theta_{\text{tot}}^\rho, \Phi_{\text{tot}}^\rho$ displays long-range correlations. The umklapp term is

$$\mathcal{H}_u = g \cos(\sqrt{6\pi}\Theta_{\text{tot}}^\rho), \quad (\text{C12})$$

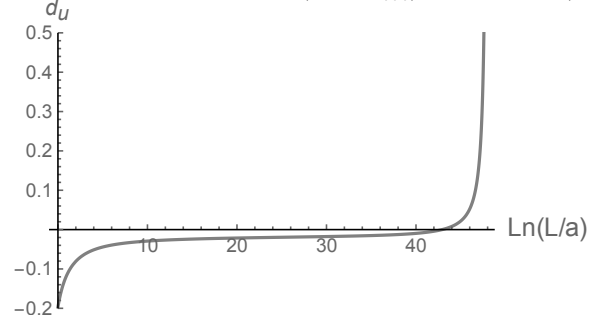


FIG. 15. Scaling dimension d_u , see Eq. (C14), for the umklapp operator given in Eq. (C13) as a function of RG-time. Here, $J/U = 0.6$ and $U = 1.5\bar{v}$ were assumed and we used Eqs. (B20) for the evaluation of the Luttinger parameters. Clearly, the umklapp operator becomes relevant before the transition to the superconducting state at $\ln(L/\bar{a}) = 48$.

which has dimension $2 - 3K_{\text{tot}}^\rho/2$ and thus appears to be relevant for $K_{\text{tot}}^\rho < 4/3$, i.e. even for attractive interactions. This seems physically inconsistent and a more appropriate treatment of the umklapp scattering for the phase C1S0 follows.

In the present case where $C_{\alpha\alpha}^\sigma \rightarrow -\infty$ for all three diagonal matrix elements, the Mott transition at half filling occurs prior to the instability to the fully gapped superconductor. Indeed, as we see from Eq. (C6), the dominant operator has the form

$$\begin{aligned} \mathcal{H}_u &= g \cos(\sqrt{6\pi}\Theta_{\text{tot}}^\rho) \times \\ &\times \left[\cos(\sqrt{2\pi}\Theta_{\text{I}}^s) \cos(\sqrt{2\pi}\Theta_{\text{II}}^s) \cos(\sqrt{2\pi}\Theta_{\text{III}}^s) \right. \\ &- \cos(\sqrt{2\pi}\Theta_{\text{I}}^s) \sin(\sqrt{2\pi}\Theta_{\text{II}}^s) \sin(\sqrt{2\pi}\Theta_{\text{III}}^s) \\ &+ \sin(\sqrt{2\pi}\Theta_{\text{I}}^s) \cos(\sqrt{2\pi}\Theta_{\text{II}}^s) \sin(\sqrt{2\pi}\Theta_{\text{III}}^s) \\ &\left. + \sin(\sqrt{2\pi}\Theta_{\text{I}}^s) \sin(\sqrt{2\pi}\Theta_{\text{II}}^s) \cos(\sqrt{2\pi}\Theta_{\text{III}}^s) \right] \\ &= g \cos(\sqrt{6\pi}\Theta_{\text{tot}}^\rho) \cos(\sqrt{6\pi}\Theta_{\text{rel}}^s) \end{aligned} \quad (\text{C13})$$

with $\sqrt{3}\Theta_{\text{rel}}^s = \Theta_{\text{I}}^s - \Theta_{\text{II}}^s - \Theta_{\text{III}}^s$. The scaling dimension of this operator is

$$d_u = 2 - 3 \frac{K_{\text{tot}}^\rho + K_{\text{rel}}^\sigma}{2}, \quad (\text{C14})$$

where

$$K_{\text{rel}}^\sigma = \frac{\sum_{\alpha} K_{\alpha\alpha}^\sigma + 2K_{\text{II,III}}^\sigma - 2\sum_{\alpha=\text{II,III}} K_{\text{I},\alpha}^\sigma}{3}. \quad (\text{C15})$$

When the operator Eq. (C13) orders prior to the C1S0 instability, an insulating C2S2 emerges, see Fig. 15.

-
- [1] J. Paglione and R. L. Greene, *Nat. Phys.* (2010).
- [2] P. J. Hirschfeld, M. M. Korshunov, and I. I. Mazin, *Reports on Progress in Physics* **74**, 124508 (2011).
- [3] A. Chubukov, *Annu. Rev. of Condens. Matter Phys.* **3**, 57 (2012).
- [4] M. Yi, Y. Zhang, Z.-X. Shen, and D. Lu, *npj Quantum Materials* **2**, 57 (2017).
- [5] H. Takahashi, A. Sugimoto, Y. Nambu, T. Yamauchi, Y. Hirata, T. Kawakami, M. Avdeev, K. Matsubayashi, F. Du, C. Kawashima, H. Soeda, S. Nakano, Y. Uwatoko, Y. Ueda, T. J. Sato, and K. Ohgushi, *Nat Mater* **14**, 1008 (2015).
- [6] T. Yamauchi, Y. Hirata, Y. Ueda, and K. Ohgushi, *Physical review letters* **115**, 246402 (2015).
- [7] S. Chi, Y. Uwatoko, H. Cao, Y. Hirata, K. Hashizume, T. Aoyama, and K. Ohgushi, *Phys. Rev. Lett.* **117**, 047003 (2016).
- [8] P. Materne, W. Bi, J. Zhao, M. Yu Hu, M. Lourdes Amigo, S. Seiro, S. Aswartham, B. Büchner, and E. E. Alp, *arXiv preprint arXiv:1810.11269* (2018).
- [9] R. Arita, H. Ikeda, S. Sakai, and M.-T. Suzuki, *Physical Review B* **92**, 054515 (2015).
- [10] N. D. Patel, A. Nocera, G. Alvarez, R. Arita, A. Moreo, and E. Dagotto, *Physical Review B* **94**, 075119 (2016).
- [11] The plot of the dispersion relation in Fig. 4 using the parameters from Ref. [10] is inconsistent with Fig. 2 b) of the same reference. In contrast to the original reference, we find that the level crossing at $k \sim \pi/3$ is avoided. Note that Figs. 2a), 3 a) and 3 b) of Ref. [10] do report an avoided level crossing near $\pi/3$ and are thus qualitatively equivalent to our plot.
- [12] M.-T. Suzuki, R. Arita, and H. Ikeda, *Phys. Rev. B* **92**, 085116 (2015).
- [13] J.M. Pizarro and E. Bascones, *arXiv preprint arXiv:1803.00282* (2018)
- [14] Y. Zhang, L. Lin, J.-J. Zhang, E. Dagotto, and S. Dong, *Physical Review B* **95**, 115154 (2017).
- [15] P. Chandra, P. Coleman, and A. I. Larkin, *Physical review letters* **64**, 88 (1990).
- [16] N. D. Patel, A. Nocera, G. Alvarez, A. Moreo, and E. Dagotto, *Phys. Rev. B* **96**, 024520 (2017).
- [17] S. Maiti and A. V. Chubukov, *Physical Review B* **82**, 214515 (2010).
- [18] A. V. Chubukov, M. Khodas, and R. M. Fernandes, *Phys. Rev. X* **6**, 041045 (2016).
- [19] L. Classen, R.-Q. Xing, M. Khodas, and A. V. Chubukov, *Phys. Rev. Lett.* **118**, 037001 (2017).
- [20] H.-H. Lin, L. Balents, and M. P. A. Fisher, *Physical Review B* **56**, 6569 (1997).
- [21] E. Arrigoni, *Physics Letters A* **215**, 91 (1996).
- [22] T. Kimura, K. Kuroki, and H. Aoki, *Phys. Rev. B* **54**, R9608 (1996).
- [23] H. Schulz, *Correlated Fermions and Transport in Mesoscopic Systems*, 81 (1996).
- [24] H.-H. Lin, L. Balents, and M. P. Fisher, *Physical Review B* **58**, 1794 (1998).
- [25] Y. Gao, W. P. Su, and J. X. Zhu, *Phys. Rev. B* **81**, 104504 (2010).
- [26] T. Ong, P. Coleman, and J. Schmalian, *Proceedings of the National Academy of Sciences* **113**, 5486 (2016).
- [27] E. König and P. Coleman, *arXiv preprint arXiv:1802.10580* (2018).